Combined Array for Research in Millimeter-Wave Astronomy

CARMA Memorandum Series #50

Astronomical Holography for CARMA Antennas

James W. Lamb and Stuartt A. Corder

California Institute of Technology

September 30, 2008

ABSTRACT

We describe the procedures for the measurement of antenna complex beam patterns using astronomical sources to derive estimates of the surface figure. After laying out the theoretical basis for the measurements, we discuss the various approximations that are made. As part of the analysis we show how the aberrations due to secondary mirror displacements are evaluated to predict the necessary adjustment of the mirror position. In a campaign in the summer of 2008, we mapped all OVRO and BIMA antennas on 41×41 grids at close to Nyquist resolution. Results from measurements show that there were some significant focus errors, which we have since corrected. We estimate that the residual errors in the surfaces are 28–50 μm after focus correction. This does not include any reduction for the estimated measurement uncertainty of about 10–20 μm, which could be subtracted in quadrature. In the OVRO antennas, most of the errors appear to be within panels, making any improvement difficult. Several BIMA antennas have sectors of panels or individual panels that should be amenable to adjustment.

Change Record

REVISION	DATE	AUTHOR	SECTIONS/PAGES AFFECTED
	REMARKS		
1.0	30-Sep-2008	JWL, SAC	All
	First release		

1 Introduction

Holographic maps of an antenna aperture field may be derived by measuring the complex beam pattern of the antenna and using the equations of wave propagation to infer the illumination field in the antenna aperture. The phase of this field is directly related to the deviation of the surface from its ideal figure, and the amplitude distribution provides information about the alignment of the feed. An interferometer is an ideal instrument for this type of measurement since it inherently has the capabilities of determining phase and amplitude

High-resolution holography maps of the surfaces of the CARMA antennas are feasible because of the wide bandwidth and high sensitivity of the λ3-mm receivers. Very high signal to noise can be achieved by scanning a few of the antennas and using the remainder as references. The multiple baselines can be used to quantify and average out some of the fluctuations due to atmospheric delay variations, as well as reducing the effects of the system noise. Preliminary work has been reported by Corder and Wright [1].

The surface figure is derived from the phase in the aperture plane, but several corrections are applied to the map to obtain the best estimate of the surface. These include some processing to reduce phase ringing due to truncation of the far-field pattern, and removal of aberrations due to secondary mirror offsets from the optimum focal position. This information is used to determining corrections for the positioning of the secondary mirror for optimum performance.

After laying out the theoretical basis for the holography analysis, we present some data obtained in the summer of 2008. All of the OVRO and BIMA antennas were measured during this campaign. None of the SZA antennas were included in the observations, but the following discussion will also be applicable to those antennas.

2 Coordinate Systems

Figure 1 shows the coordinate system used in this analysis. Note that this coordinate does not conform to the convention for antennas where the *x*-coordinate is in the elevation direction and the *y*-axis is in the azimuth direction. Here we use the non-standard system with the *x*-axis parallel to the elevation axis, the *y*-axis in the cross-elevation direction (vertically upward when the antenna is pointed at the horizon), and the *z*-axis in the boresight direction, pointing to the source, forming a right-handed system. On the sky we also use a spherical coordinate system $(\theta\ ,\phi)$ as shown.

When the antennas are scanned to measure the beam patterns, the offsets are ΔEl, which is positive moving toward the zenith, and ΔAz, which is positive for clockwise rotations about the vertical axis when viewed from above. The CARMA control system command for the azimuth offset actually takes a value corresponding to $\Delta Az/\cos El$ so that, in the small angle approximation, a given commanded offset value results in the same magnitude of angular offset on the sky in both directions. Applying a positive elevation offset to the antenna puts the source in the negative y coordinate in the beam, so this sign has to be reversed to be consistent with the antenna coordinate frame. In contrast, moving the antenna by a positive azimuth puts the source in the positive x direction in the beam, so no sign reversal is required.

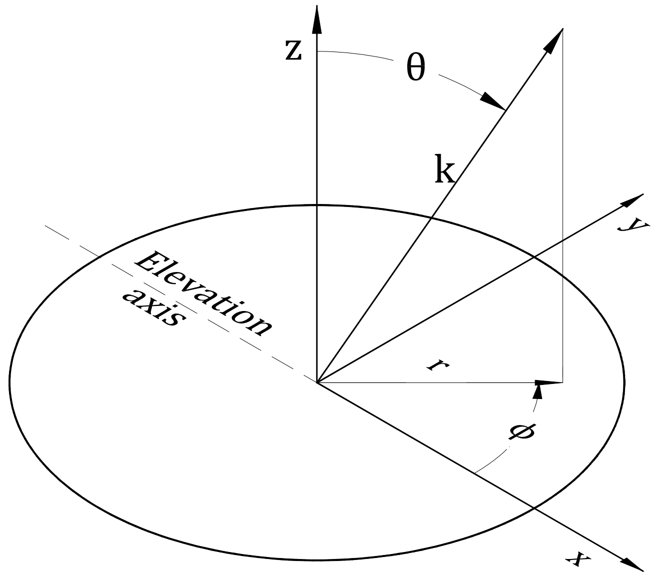

Fig. 1.— Coordinate system used for the beam and aperture plane. The y-axis points vertically up when the antenna is at the horizon.

3 Theoretical Foundations

3.1 Relationship between Aperture Field and Far-Field Patterns

As usual, we treat the antenna as a transmitter. If the electric field in the aperture at some wavelength λ is polarized in the x-direction with a distribution $E_x(x, y)$, then the field at some large distance ρ from the aperture is given by [2]

$$\vec{E}(\rho, \theta, \phi) \approx \frac{i \exp(-ik\rho)}{\lambda r} \left(\hat{\theta} \cos \theta - \hat{\phi} \sin \theta \cos \phi\right) F(k \sin \theta \cos \phi \,, k \sin \theta \sin \phi \,) \,, \tag{1}$$

where the plane wave spectrum is

$$F(k_x, k_y) = \int_{-\infty}^{\infty} \int_{-\infty}^{\infty} E_x(x, y) \exp\left[i\left(k_x x + k_y y\right)\right] dx \, dy \,, \tag{2}$$

k is the wavenumber

$$k = \frac{2\,\pi}{\lambda} , \tag{3}$$

corresponding to the wave vector

$$\vec{k} = \hat{x} k_x + \hat{y} k_y + \hat{z} k_z \,, \tag{4}$$

and the hat symbol (̂) indicates a unit vector in the direction of the coordinate it modifies. Corresponding expressions apply to the y-polarized component.

For interpreting the holography results we apply some simplifying assumptions. Firstly, we assume a small-angle approximation for the far field, $\theta \ll 1$. Secondly, we assume that the polarization of the field is identical at all points in the aperture. These assumptions allow us to treat the field as a scalar and we do not need to consider what the actual polarization is for the holography measurements. Since we are not concerned with the absolute magnitude or phase of the far field we may drop the first term in (1) and write the scalar equivalent of the far field (suppressing the radial distance coordinate) as

$$E(l,m) \approx F(kl,km)\,, \tag{5}$$

with new coordinates $l = \sin\theta\cos\phi$ and $m = \sin\theta\sin\phi$, which are the direction cosines in the cross-elevation and elevation directions respectively. Combining (5) with (2) gives

$$E(l,m) \approx \int_{-\infty}^{\infty}\int_{-\infty}^{\infty} E_x(x,y)\exp[i(lx+my)]\,dx\,dy, \tag{6}$$

which is recognizable as a two-dimensional inverse Fourier transform. We ignore any constant factors in the transforms since we are not interested in absolute power levels. Application of the forward Fourier transform (again ignoring constant prefactors) allows recovery of the aperture field if we have complete knowledge of the far-field complex beam pattern.

3.2 Measurement of Antenna Beam Pattern

Maps of the complex beam of an antenna are easily measured with an interferometer. If one antenna is scanned over an unresolved astronomical source the output from the correlation with another antenna tracking the source is proportional to the complex beam pattern of the scanned antenna. Normally the output of the correlator is proportional to power since it is the product of voltages from separate antennas. In the case of holography, the voltage from one antenna is unvarying, so the product is directly proportional to the moving antenna's voltage response. If the source is resolved by the interferometer the main consequence is that the visibility amplitudes are reduced on longer baselines. Although this factor is time varying as the source is tracked, it is easily calibrated out.

Aperture antennas have a well-defined extent so that their inverse Fourier transform need be sampled only at discrete interval corresponding to the Nyquist rate. For holography the angular sampling of the beam for an aperture of diameter D has a Nyquist interval of

$$\Delta\theta_{Ny} = \frac{\lambda}{D}\,. \tag{7}$$

Again, this contrasts with normal astronomical measurements, which require a sampling interval of half this. This can be understood by considering either that the spatial frequencies are doubled by squaring the amplitude pattern to get power, or by recognizing that the response in the visibility (aperture) plane is proportional to the autocorrelation of the aperture field which has a scale size of $2D$.

To be able to use standard fast Fourier transforms (FFT), the antenna pattern should be sampled on a uniform rectangular grid in the space defined by the arguments of the function $F(kl,km)$, i.e., in direction cosines. In the CARMA system, offsets may currently be commanded in RA and Dec coordinates, or in azimuth and elevation offsets. The latter is the more natural for beam mapping since it is closely related to the antenna coordinates. If the source is being tracked by the array with azimuth and elevation coordinates Az and El, then the direction cosines for the source in the antenna aperture coordinates are

$$l = \cos El \sin \Delta Az$$
$$m = -\sin \Delta El \,(\sin^2 El + \cos^2 El \cos(\Delta Az)) + \cos \Delta El \sin El \cos El \,(1 - \cos \Delta Az) \tag{8}$$

Expanding these to lowest order in ΔAz and ΔEl yields the expected expressions

$$l = \Delta Az \cos El$$
$$m = -\Delta El \tag{9}$$

The errors in these are small and can be ignored for most measurements. An extreme case is shown in Fig. 2, which compares the assumed and exact sampling points for an OVRO antenna at a wavelength of 10 mm, a 64 × 64 Nyquist sampled grid, and an elevation of 70°. The maximum error is ~4.5 arcmin, compared with the Nyquist interval of 3.3 arcmin. The SZA control system has the offsets implemented in the (l, m) coordinate system, which is more important for the small antennas since the Nyquist size, and hence the grid size, are proportionately larger.

All the data in this memo were taken with the approximate expressions. In the CARMA control system the values supplied to the `offset(az, el)` command are `az` $= \Delta Az$ and `el` $= El \cos \Delta$El, in arcmin.

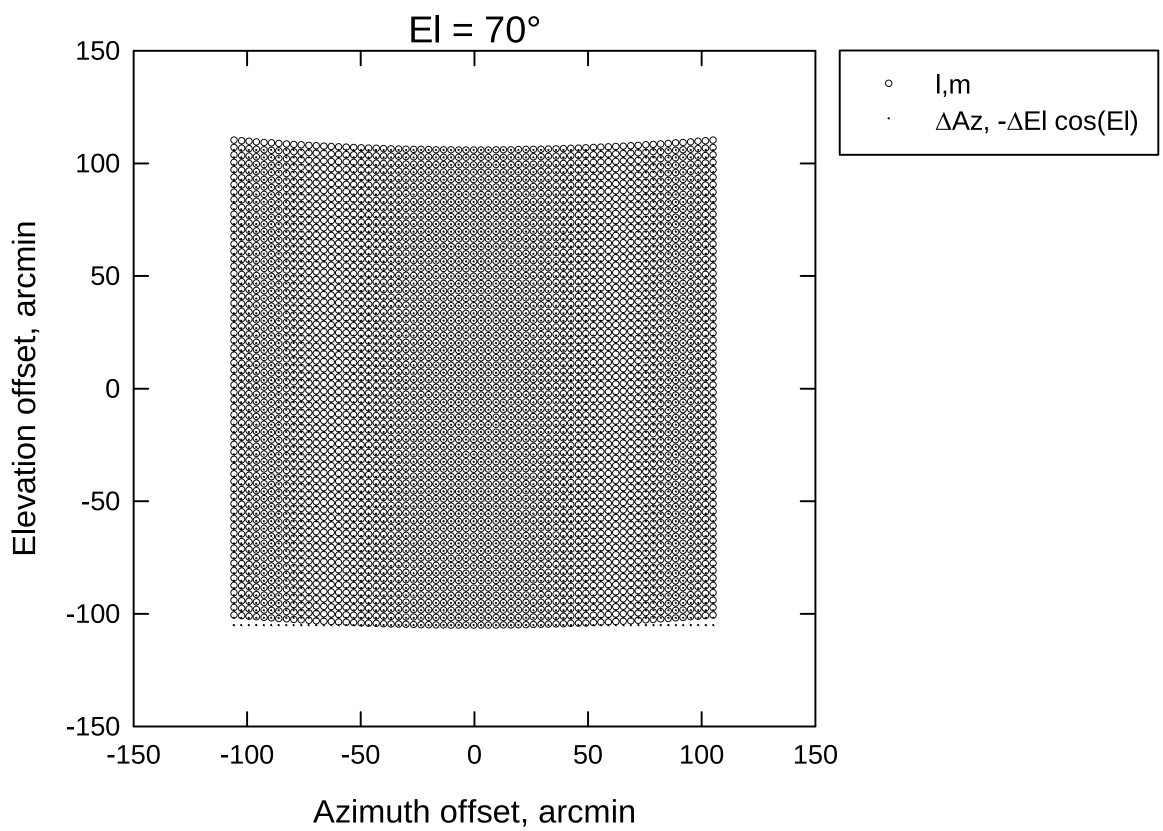

Fig. 2.— Comparison of actual and ideal coordinates. Ideally the grid for the measurement should be rectangular in (l, m) space, but the actual coordinate system has some distortion that is not corrected.

3.3 Derivation of Surface Figure from Complex Beam Pattern

Several steps are required in processing the far-field data to produce an estimate of the surface figure of the antenna. The importance of these depends on various factors, particularly on the resolution of the maps (or, equivalently, the extent of the far-field beam map), the observing wavelength, and the antenna diameter and focal ratio.

3.3.1 Phase Reference

Firstly, we consider the phase reference for the measurement. The interferometer engine for the array is designed to ensure precise compensation for the geometric delay, effectively placing the apertures of all the antennas on the same phase plane for a source on axis. When one antenna is rotated θ from the reference pointing direction, with the center of rotation (at the Az/El intersection) at a distance d_a behind the aperture it has an additional delay relative to the reference of

$$\delta d = d_a(1 - \cos\theta)\,, \tag{10}$$

which may be removed from the beam-pattern before transforming to the aperture plane. For small maps of the larger antennas this is a negligible effect, but for a 30 GHz observing frequency on the SZA antennas and maps of order 41 × 41 points there is a correction of up to ~60° to the phase. In principle, the distance d_a can be adjusted to map the field at any depth in the primary reflector, but it is generally sufficient to set it equal to the mean distance from the dish to the axis.

3.3.2 Beam Map Truncation

Taking the Fourier transform of the far field sampled out to $\pm\theta_{max}$ is equivalent to convolving the true aperture field with

$$f(x, y) = \mathrm{sinc}\left(\frac{x}{\lambda\theta_{max}}\right)\,\mathrm{sinc}\left(\frac{y}{\lambda\theta_{max}}\right) \tag{11}$$

Mapping over a circular region has a corresponding $\mathrm{bessinc}(r/\lambda\theta_{max})$ convolving function. At the edge of the primary reflector there is a step discontinuity in the aperture field, and convolving this with (11) produces phase ripple that can mask the phase errors due to the surface. A partial amelioration for this can be achieved by extending the beam pattern synthetically as follows. First pad out the far-field data with zeros in some large area surrounding the measured data and then transform the data to the aperture plane. This will have the effect of interpolating the aperture plane on to a finer grid which will have non-zero values in the blocked regions (outside the aperture, and within the strut and central blockage). Those points known to be blocked are set to zero and the far-field reconstituted by the appropriate transform, which will create diffraction lobes outside the measured map area. Now the values over the observed area of the grid are replaced by the original measured data, and a new estimate aperture field obtained by transforming back to the antenna coordinates. This procedure may be repeated iteratively to obtain a converged result that is consistent with both the measured beam pattern and the known blockage.

3.3.3 Pointing and Focus Removal

The third step is to remove the pointing and focus terms from the phase map. The path error in the map relative to the mean value may be written as

$$P = P_{\alpha x} + P_{\alpha y} + P_{\Delta x} + P_{\Delta y} + P_{\Delta z} + P_{surf} \tag{12}$$

Where P is the total path error, $P_{\alpha x}$ and $P_{\alpha y}$ are the path error due to a tilt of the wavefront (i.e., a pointing error) by an angle α about the x and y axes respectively, $P_{\Delta x}$, $P_{\Delta \mathrm{y}}$, $P_{\Delta z}$ are the coma and spherical aberration path errors due to a movement of the secondary by Δx, Δy, and Δz along the respective axes, and P_{surf} is the path error due to surface figure deviations from a paraboloid. Each P is a function of the location in the aperture, $P = P(x, y) = P(r, \phi)$. Apart from the surface error, all the terms are linearly dependent on the source of the error so they may be written, for example, as $P_{\Delta x} = \Delta x\, p_{\Delta x}$, where $p_{\Delta \mathrm{x}}$ is a normalized error per unit offset of the secondary in the *x* direction.

Eq. (12) can be written more generally as

$$p(x, y) = \sum_i c_i p_i(x, y)\,. \tag{13}$$

Each coefficient corresponds directly to a physical misalignment. Normally these terms are not orthogonal, so, for example, a lateral displacement of the secondary will contribute a pointing term as well as a coma term. However, if the path errors are cast appropriately, these terms may be suitably orthogonalized. When the functions are p_i are orthogonal[1] we have the usual property that

$$\begin{aligned} \iint_A p_i(x, y) p(x, y) dx\, dy &= \sum_j c_i \iint_A p_i(x, y)\, p_j(x, y) dx\, dy \\ &= c_i \iint_A p_i^2(x, y) dx\, dy\,. \end{aligned} \tag{14}$$

Rearranging this gives an explicit expression to project out the coefficients

$$c_i = \frac{\iint_A p_i(x, y) p(x, y) dx\, dy}{\iint_A p_i^2(x, y) dx\, dy}\,. \tag{15}$$

Often Zernike polynomials are used to represent the aberrations, but in this case we choose to use the Ruze approximations that give the precise form of the wavefront distortion, directly related to the secondary displacements. These expressions are orthogonal to each other provided the mean value is removed (see Appendix). When written appropriately, the coefficients are the physical motions of the secondary in millimeters.

3.3.4 Secondary Mirror Diffraction

Edge diffraction of the feed illumination causes amplitude and phase ripple within the perimeter of the aperture. Using the expressions for the scatter pattern of the secondary derived by Rusch [3] we can calculate the resulting field in the aperture. From the results presented in Fig. 2 we can see that the amplitude of the phase ripple is about 20° peak to peak at 95 GHz (~90 µm equivalent peak-to-peak surface error). At the periphery, the period of the ripple is about 0.6 m which would start to be resolved—particularly on the diagonals—for maps of about 35 points in each direction. Since there are a couple of periods across any panel this ripple will in practice cause only a small error in setting the panel, even if it is resolved. The overall RMS surface error equivalent error for the phase ripple is 19 µm unweighted, and 14 µm weighted by the illumination amplitude. This would be included as part

[1] By definition, the surface error, P_{surf}, is orthogonal to the other terms since we can remove all components of the surface error that match the focus aberrations.

of the diffraction efficiency at this frequency, but should not be included as part of the surface error measurement.

The period of the ripple scales as the square root of the wavelength, and the equivalent surface RMS directly as the wavelength. If holography data are taken at 30 GHz, these effects will be significant and need to be taken into account. This can be done with sufficient precision by removing the predicted phase variation, convolved with the resolution function, from the measured maps.

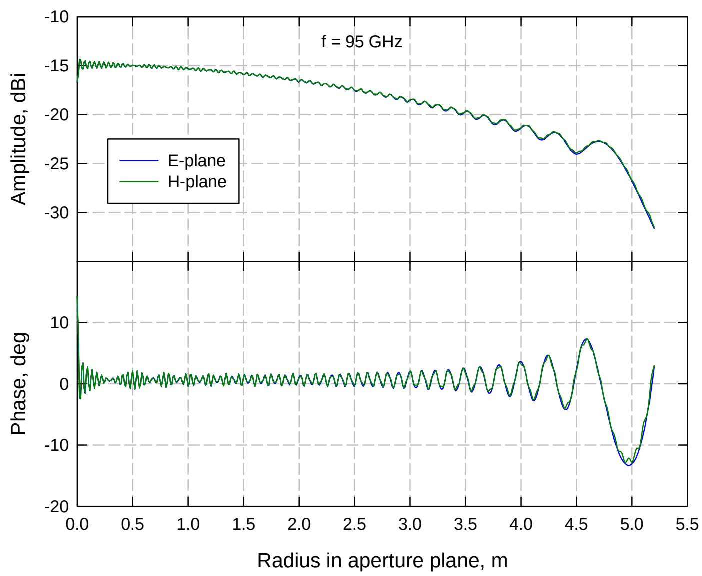

Fig. 3.— Amplitude and phase of illumination of aperture by an idealized feed at the secondary focus for illumination at 95 GHz.

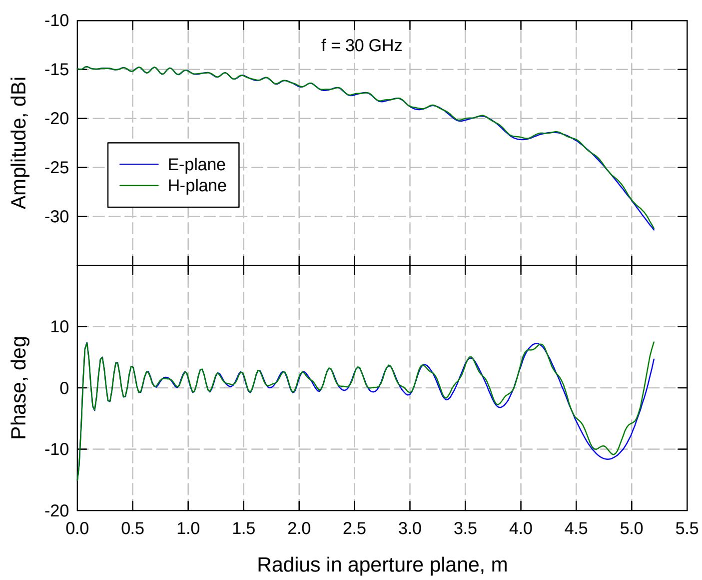

Fig. 4.— Amplitude and phase of illumination of aperture by an idealized feed at the secondary focus for illumination at 30 GHz.

3.3.5 Surface Error

Antenna surface quality is conventionally given in terms of an effective surface RMS error, ϵ, which is defined as half the RMS path length error, and sometimes referred to the half-wavefront or axially resolved surface error. This is the definition that we use in this memo, but the deviations of the reflector normal to the surface will be somewhat larger. Simple geometry shows that the effective axial error, Δz, is related to the deviation along the normal, Δn, by

$$\Delta z(r,\phi) = \Delta n(r,\phi)\cos\tfrac{1}{2}\theta_p, \tag{16}$$

where θ_p is the angle of the ray from the focus relative to the antenna axis. Depending on the particular antenna type, the adjustment of the panel mounting screws may have a different relationship to the local surface error.

Ruze [4] demonstrated that under certain conditions the efficiency of the antenna is reduced by a factor

$$\eta_{Ruze} = \mathrm{e}^{-\left(\frac{4\pi\epsilon}{\lambda}\right)^2}. \tag{17}$$

In practice this formula works well for a much less restrictive range of surface error profiles than in considered by Ruze and is generally used without particular regard to what the distribution of errors actually is.

4 Observation and Analysis

4.1 Data Acquisition

Data are acquired using the `ct001_holography.obs` observing script. This has several parameters such as the source, grid size, and test antenna(s). Observations start with pointing all antennas on the source, and then the test antennas are stepped in Az and El. The angular step size o the sky defaults to $(1-1/N)\lambda/D$ at the shortest wavelength across the observing band, slightly less than the Nyquist step so that there is a half pixel border in the resulting aperture map.

At the start of the observations, radio pointing is done on the source to be used for the holography data. One or more antennas that are to be measured are scanned in a rectangular grid while the remainder track the source to provide the reference phase. Scans are made row by row, starting at the lowest elevation. Before each row in the map a measurement of the central pointing is made, and then a row is scanned at constant elevation. After the last row a final central observation is made. Noise integrations are made after every ten source integrations as a general check of the system.

An observing log is written by the observing script (http://cedarflat.mmarray.org/array/holography/), and the data are filled into a Miriad data set.

4.2 Analysis

Once the Miriad data are copied to a local directory they may be extracted using the python script `extractHoloData.py` (in the `scripts/python/arrayHealth/` directory). The python script determines the antennas being tested and the offset grid. It uses a Fortran program, `uvhol`, based on `uvlist` and `uvindex` to convert the ‘visibility’ data to ASCII format. Before the data are converted for processing they are calibrated in Miriad using `mfcal`. All the visibilities with zero azimuth and elevation offset are selected as calibration observations, typically using one of the test antennas as the phase reference. Passbands and complex gains are determined from these, and then applied to all baselines with the test antennas.

All visibilities are extracted for baselines with the test antennas. These are converted to amplitude and phase. **If the test antenna number is lower than the reference antenna number, the visibilities are conjugated**. This ensures that the phase definition is consistent with the analysis outlined above. Data are then written into text files, one for each antenna and each spectral window.

All of the detailed analysis is carried out using Mathcad worksheets, in a couple of stages.

4.3 Processing Single Window Data

Data for a single antenna and single window (all baselines) are read into a Mathcad worksheet, and amplitudes and phases for the central pointings are plotted for all baselines. These should be close to $1.0\angle 0°$ since they were calibrated in Miriad. Reference antennas that have suspect quality may be removed from the selection set. The central pointings are spline interpolated to correct the map points between reference measurements, but this correction is only a small change relative to the Miriad calibration that has already been applied.

The sign of the elevation offset is changed to match the coordinate system used for the analysis as described in Sec. 2.

All the beam patterns are averaged together. As a measure of fidelity, the individual maps are differenced with the average and the RMS residual reported. If any map is a significant outlier it may be removed from the data set. Otherwise, the maps are re-averaged, weighted by the inverse of the variance relative to the mean.

Eq. (10) is applied to the averaged far-field pattern phases, and a Fourier transform is used to generate the initial estimate of the aperture field. For this the Mathcad function `CFFT()` is used since it does a two-dimensional complex transform with the appropriate sign for the exponential. Since Mathcad assumes a starting index of zero for transforms, it is necessary to rearrange the data by swapping quadrants to put the centre of the map at (0, 0). After the transform the quadrants are swapped back. The far-field and aperture field maps may be inspected visually for any anomalies, such as missing data points.

Following the prescription in Sec. 3.3.2, the data are interpolated on to a higher resolution grid with the known blockage imposed on the aperture pattern. The data are then written to an ASCII file in the form of (x, y) coordinates in the aperture plane, and path error in μm. A second file is written with the amplitudes, normalized to a maximum of unity. This process is repeated for the remaining spectral windows.

4.4 Combination of Spectral Window Data

In a second Mathcad worksheet, all the spectral windows (typically 6) for a given antenna are read in and plotted for comparison. Since the different windows are at different frequencies, the grids, which have identical spacing in wavelengths, have different sizes in units of meters. They are therefore resampled using a two-dimensional cubic spline fit on to a common grid before being averaged.

Linear terms are fitted in x and y to the averaged data to determine the pointing offsets, if any, and these are removed from the path length error. Next the secondary mirror x, y, and z focus errors are determined according to Sec. 3.3.3. Generally the map data have artifacts at the edges of the aperture, at the central blockage, and near the secondary mirror support shadows that appear as spikes. We therefore chose to ignore values close to these boundaries when fitting the focus and calculating residual surface errors.

When the pointing and focus terms have been removed from the path error the RMS value is found and divided by two to produce the surface accuracy estimate. The final map is written out to a text file. A value for astigmatism can also be extracted, but this is not removed from the path length error map since it cannot be reduced by refocusing the secondary.

Another Mathcad worksheet is used to form the average of all the amplitude maps, also resampled on to the same grid.

5 Results—Summer 2008

5.1.1 Observations

During the summer of 2008, measurements were made of all OVRO and BIMA dishes in nine observing sessions, including initial testing. This was done in the *D* configuration, so all the baselines were reasonably short (<150 m). Observing conditions typically had good phases (≤200 μm on 100 m baseline) and reasonable to good opacities ($\tau_{225} = 0.2 - 0.6$). Observations were carried out with an LO frequency of 95.0 GHz, IF center frequencies of 1.75, 2.25, and 2.75 GHz, and bandwidths of 500 MHz. The source was the quasar 3C454.3 (22:53:57.7 RA, +16:08:53.6 Dec) which was particularly bright (25–33 Jy), and up during the night. All observations were made between about 30° and 68° elevation (transit).

Table 1: Summary of holography observations for summer 2008.

Ant.	Run	Map size	Step Size arcmin	Comments
C1	30-Jun-08	31x31	0.491	Oversampled; out of focus (–1.97 mm)
	10-Jul-08	31x31	0.491	Oversampled
	22-Jul-08	31x31	0.982	
	3-Aug-08	41x41	0.990	
C2	3-Aug-08	41x41	0.990	
	29-Aug-08	41x41	0.990	Refocused
C3	11-Aug-08	41x41	0.990	
C4	11-Aug-08	41x41	0.990	Missing data near main beam
	29-Aug-08	41x41	0.990	
C5	27-Jul-08	41x41	0.990	Large changes in on-axis amplitudes; Only 2 bands
	29-Aug-08	41x41	0.990	
C6	27-Jul-08	41x41	0.990	Band 3 missing
C7	20-Aug-08	41x41	1.687	
C8	19-Aug-08	41x41	1.687	
C9	20-Aug-08	41x41	1.687	
C10	19-Aug-08	41x41	1.687	
C11	20-Aug-08	41x41	1.687	
C12	19-Aug-08	41x41	1.687	
C13	20-Aug-08	41x41	1.687	
C14	19-Aug-08	41x41	1.687	
C15	20-Aug-08	41x41	1.687	

Initial maps were made on grids of 31×31 points on C1, with the first two maps oversampled by a factor of two. The integration time was 10 s per point. Later maps were on 41×41 grids sampled by one pixel over Nyquist, and with 5 s integration per pointing. These observations took about 5.5 hr. A summary of the observations, giving the dates and map parameters is given in Table 1.

5.2 Verification of Signs

Although the signs for phase and offset were carefully checked *a priori*, some additional tests were made with the measured data. The hardest to determine is the sign of the phase since there is an arbitrary choice for this, and the correlator and Miriad differ in their definitions. For the first map, the secondary mirror on C1 was displaced by about 2 mm towards the primary. As verified by ray tracing, this should advance the wavefront at the center of the aperture relative to the edge, which is a positive phase as defined in the analysis. The difference between the 30 June and 10 July data derived from the maps gave a focus change of –1.84 mm, compared with the actual value of –1.97 mm, an error of about 7 %.

The inverted 'Y' of the BIMA secondary support structure was used to check that the sign of the elevation coordinate was correct. This relies on the phase definition also being correct since phase reversal rotates the aperture pattern 180° about the *z*-axis. A final check was to compare the maps with earlier ones made by Dick Plambeck using the transmitter and identify some common features

5.3 Data Quality

Comparisons of the different baselines and frequency windows are useful to evaluate the statistical limits on the data quality. All windows have independent radiometer (additive) noise, but the atmospheric fluctuations (multiplicative noise) will be fully correlated between windows and partially correlated between baselines. By splitting data up according to baseline or window we can try to distinguish the magnitude of the two sources of error.

As a first order check, one of the data sets was analyzed for each baseline. The estimated surface error is shown as a function of baseline length in Fig. 5. No clear evidence is visible for any dependence on either baseline length or reference antenna area even though there is a factor of three variation in both quantities.

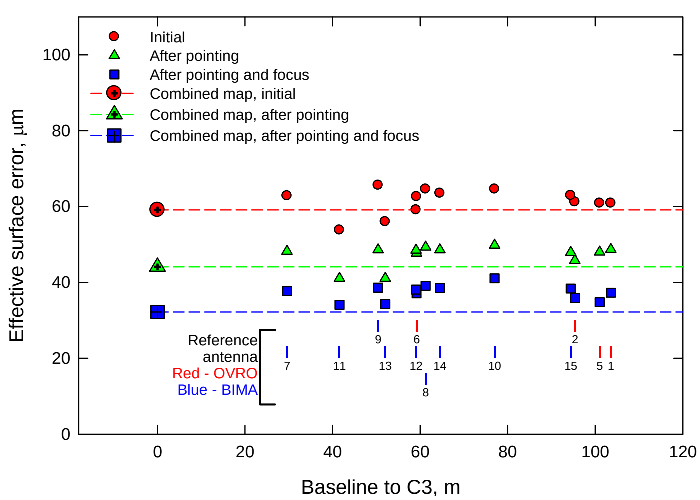

Fig. 5.— Relationship of surface error measurement to baseline length and antenna type.

Some estimate of the errors in the measurements may be made as follows. Assume that the true surface error of the antenna is ϵ_0 and that the RMS value of the measurement noise in a single map is σ, then the expected measurement for the surface error in that map, ϵ_1, is

$$\epsilon_1^2 = \epsilon_0^2 + \sigma^2 \, . \tag{18}$$

If n maps with the same RMS error are averaged together, the estimated surface error, ϵ_n, will be

$$\epsilon_n^2 = \epsilon_0^2 + \sigma^2/n \, , \tag{19}$$

assuming all maps have the same value of σ. Solving (18) and (19) we can separate out the true surface error and the measurement error:

$$\epsilon_0^2 = \frac{n\epsilon_n^2 - \epsilon_1^2}{n-1} \, , \tag{20}$$

and

$$\sigma^2 = \frac{\epsilon_1^2 - \epsilon_n^2}{1 - 1/n} \, . \tag{21}$$

ϵ_1 can be taken as the average over all the maps.

Results for C3 from 11 Aug 2008 are shown in Table 2 and Table 3.

Table 2: RMS surface error estimated for C3 from each baseline with a reference antenna. Each map has all six spectral windows averaged together.

Baseline	Map RMS, µm
1–3	37.3
2–3	35.9
3–5	34.8
3–6	37.1
3–7	37.7
3–8	39.1
3–9	38.6
3–10	41.1
3–11	34.4
3–12	38.1
3–13	34.3
3–14	38.5
3–15	38.4
ϵ_1	37.3
ϵ_n	32.2
ϵ_0	31.7
σ	19.5

Table 3: RMS surface error estimated for C1 from individual spectral windows. Each window has all baselines averaged together.

Window	Map RMS, µm
1	55.8
2	33.0
3	31.9
4	33.8
5	32.1
6	33.7
ϵ_1	36.7
ϵ_n	32.2
ϵ_0	31.2
σ	19.3

From the results in Table 2, the error in a map for a single baseline and single window is estimated to be $\sqrt{6} \times 19.5 = 47.8$ µm, while the Table 3 results suggest a value of $\sqrt{15} \times 19.3 = 74.7$ µm. It is not clear what this discrepancy is due to, but it possibly results from assuming that all the maps have the same noise, which is clearly not the case. The RMS error in the final map is estimated to be 5–10 µm.

Another test of the data is the repeatability of maps taken at different times. Figure 6 shows two maps of C2 taken on 3 Aug 2008 and 29 Aug 2008 after the pointing and focus effects have been removed. Most of the features can be clearly discerned on both maps, and the difference map shows some slightly significant systematic structure. The difference map has an RMS of 20.4 µm, which can be attributed as 14.4 µm per map. This is significantly larger than the expected from the analysis done for a single map of C1 as discussed above. It may be that there is some systematic variation between the maps resulting from the different elevation coverages, as shown in Fig. 7.

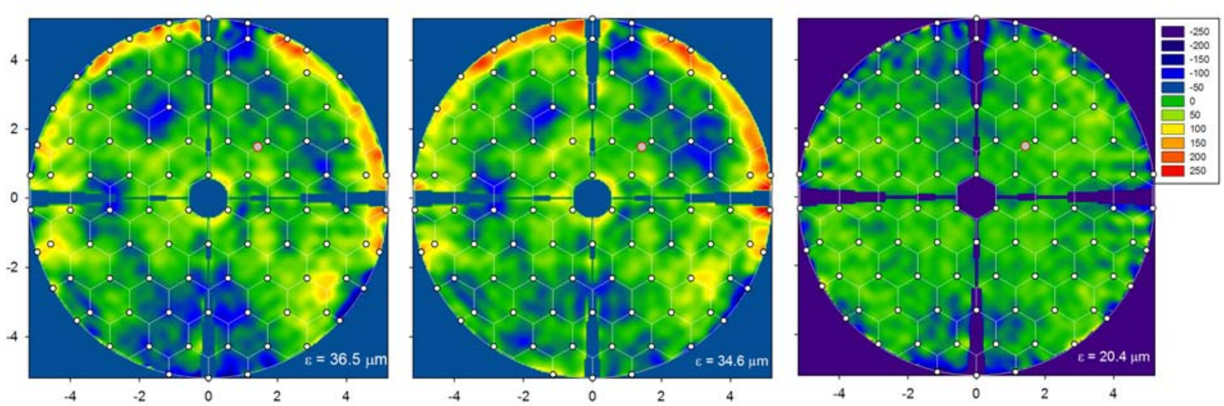

(a) (b) (c)

Fig. 6.— (a) Surface error map for C2, 03 Aug 2008, (b) surface error map, 29 Aug 2008, and (c) difference between (a) and (b). Maps are as viewed from the front of the dish, with positive errors being high, and negative ones low.

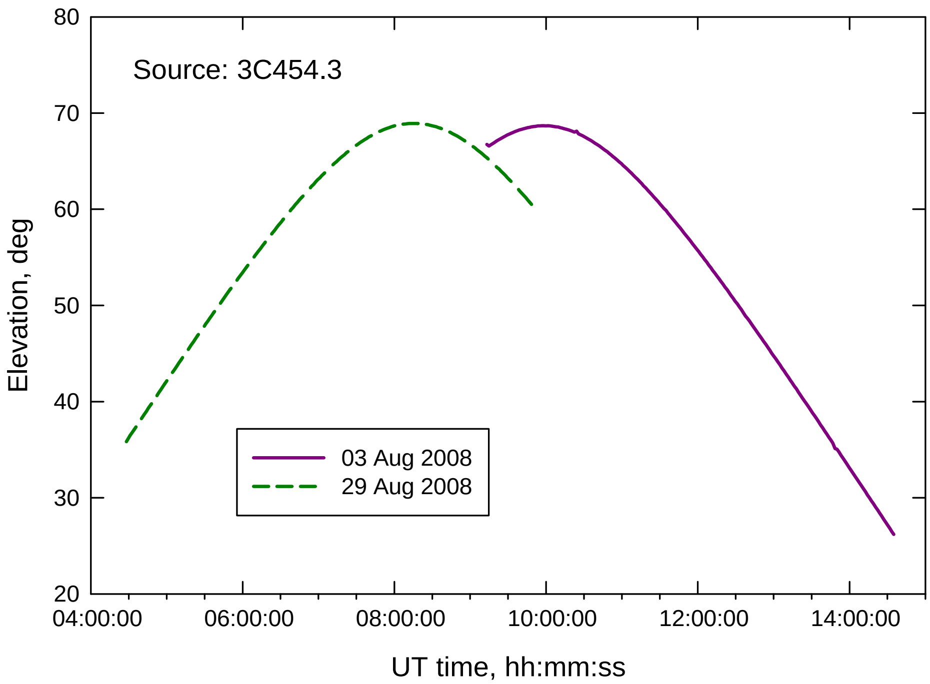

Fig. 7.— Elevation range covered by maps of 03 and 29 Aug 2008.

C4 also was also measured on two occasions. Fig. 8 shows the two maps and their difference. In this case there is a lot of structure corresponding to the panel pattern and this shows up clearly in the two maps. In the difference map most of this structure is eliminated and only some large scale structure with a somewhat astigmatic form remains. This is not real but results from missing data in the beam map. A pixel one grid point diagonal off the center was missing and its value was replaced by that of the diagonally opposite pixel. Most of the error in the difference map appears to be systematic. If we assume that the errors are equally divided between the systematic large-scale error and random noise in the measurement then the systematic contribution would be 23 μm and the noise 16 μm from each of the maps. The quadrature difference between the RMS values for the two maps indicates that the systematic error should be only 10 μm, however. This would be consistent if the noise in *each* map is 22 μm, so the measurement errors in the maps are probably somewhere between 16 and 22 μm.

In the values we quote for the surface RMS we do not account for the estimated noise contribution, partly since it does not have a well defined value. This would in any case lead to only a small reduction of the surface error estimate by a few microns.

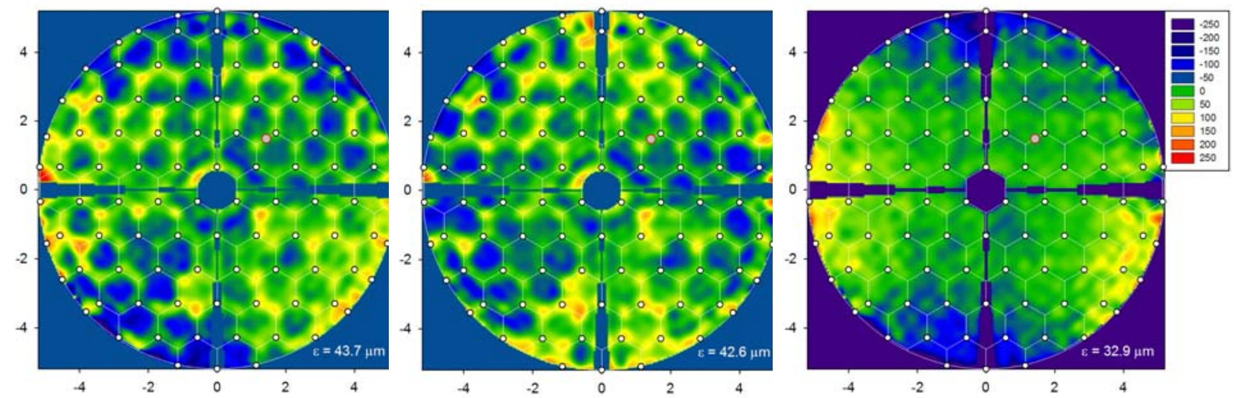

(a) (b) (c)

Fig. 8.— (a) Surface error map of C4, 11 Aug 2008, (b) surface error map of C4, 29 Aug 2008, and (c) difference between (a) and (b).

5.4 Amplitude and Surface Error Maps

The following maps are derived from the best observation obtained for each antenna. In most cases there was only a single observation made. The data were all taken on 41×41 grids with the sampling interval given by (7). Amplitude maps are normalized to their maximum value. Surface error maps are plotted on a scale from –250 to 250 μm.

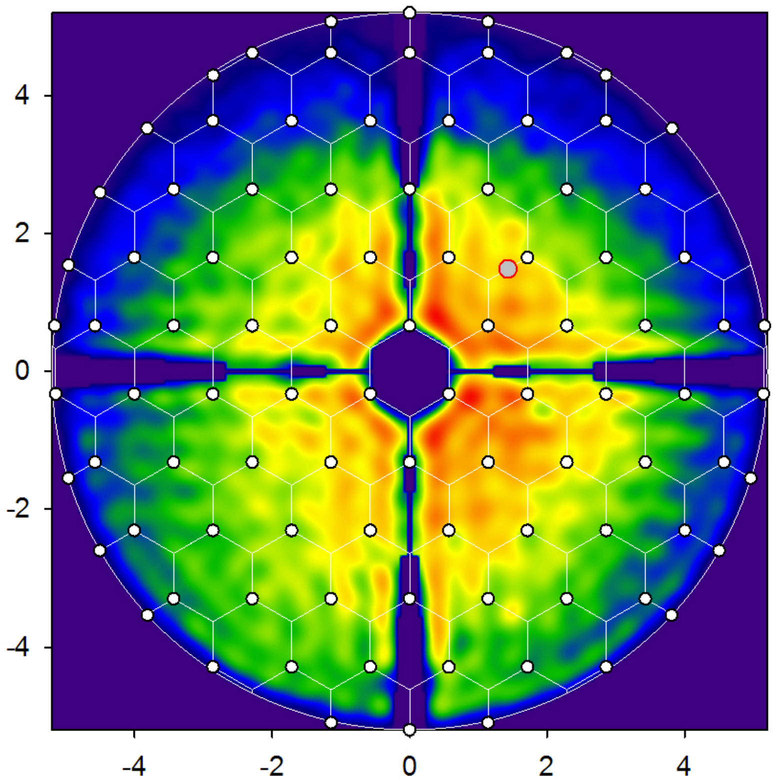

C1 field amplitude

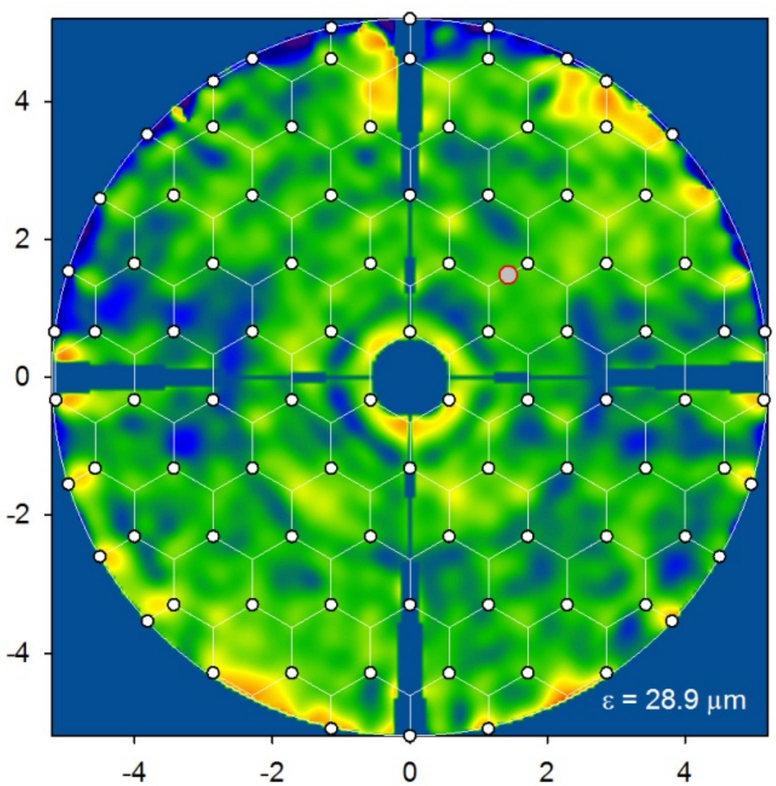

C1 surface error

Fig. 9.— Maps of the field amplitude distribution and surface error for all the antennas. The same scale is used for all surface the maps, from –250 μm to +200 μm.

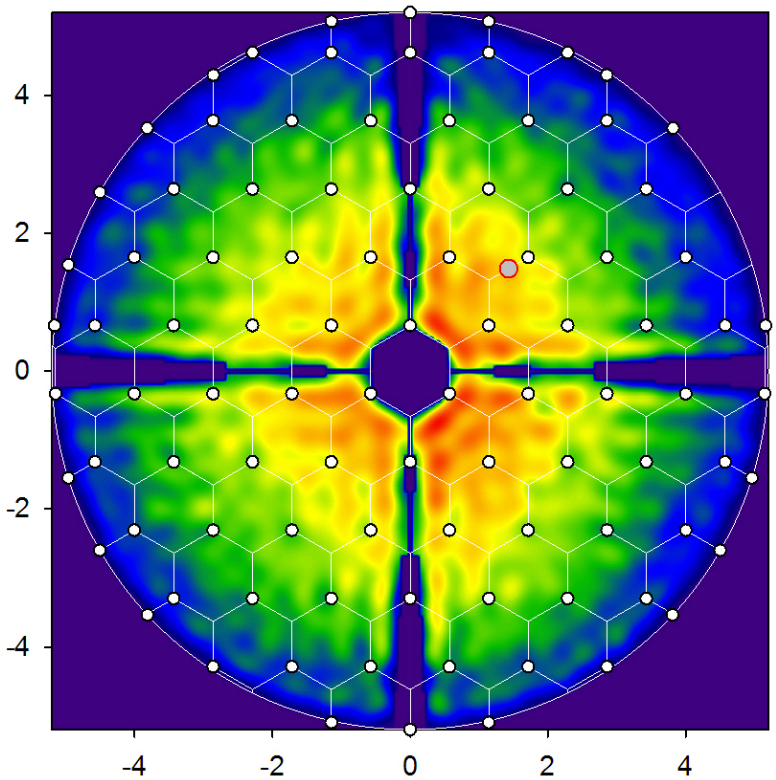

C2 field amplitude

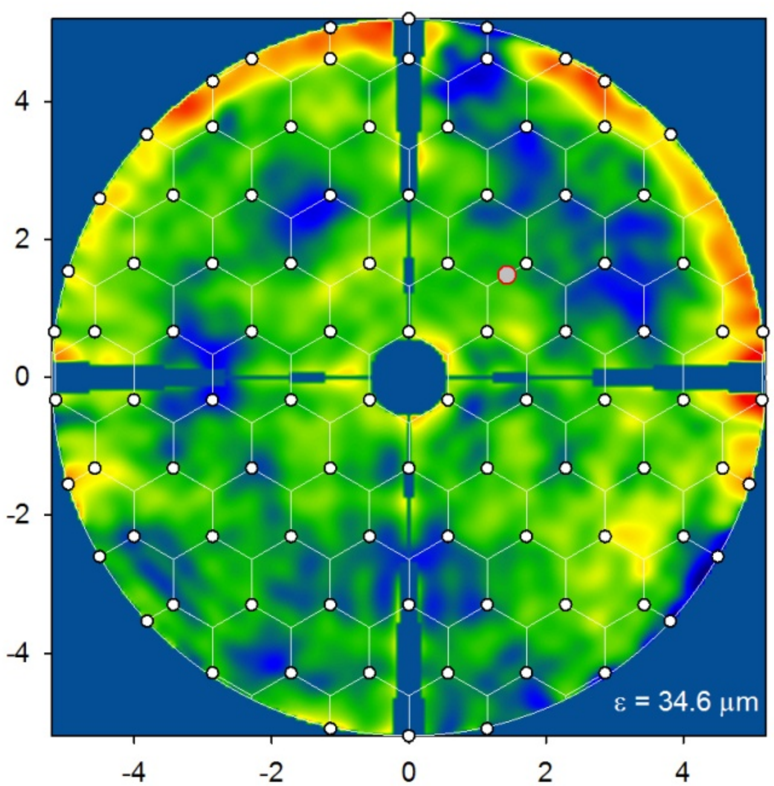

C2 surface error

Fig. 9.— Cont'd

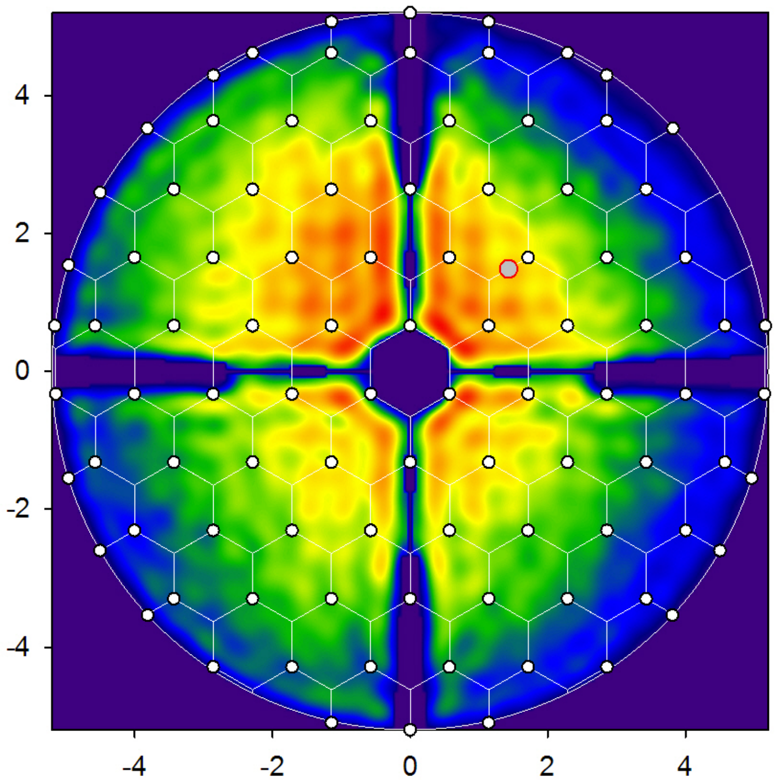

C3 field amplitude

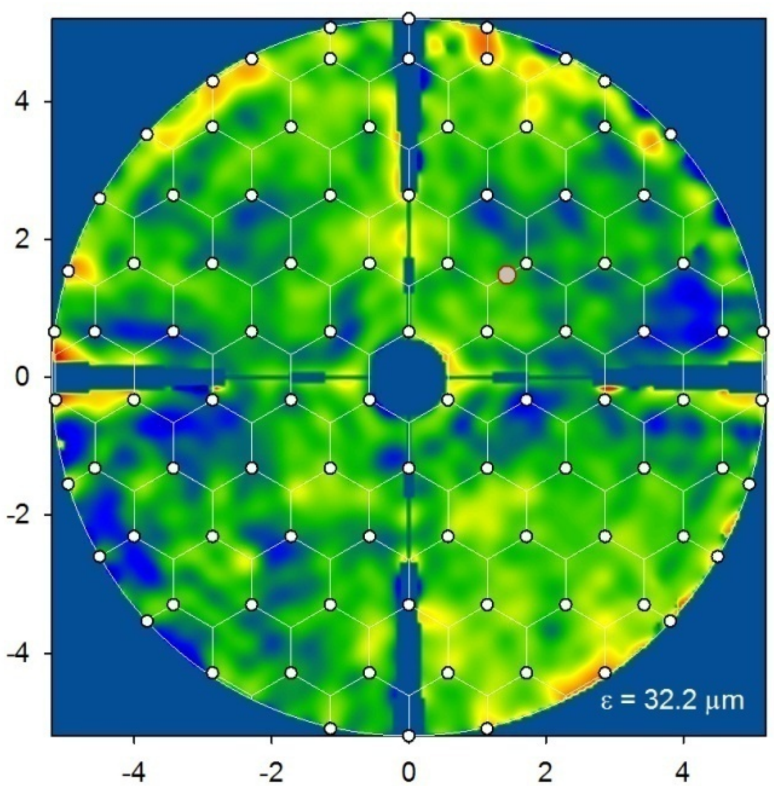

C3 surface error

Fig. 9.— Cont'd

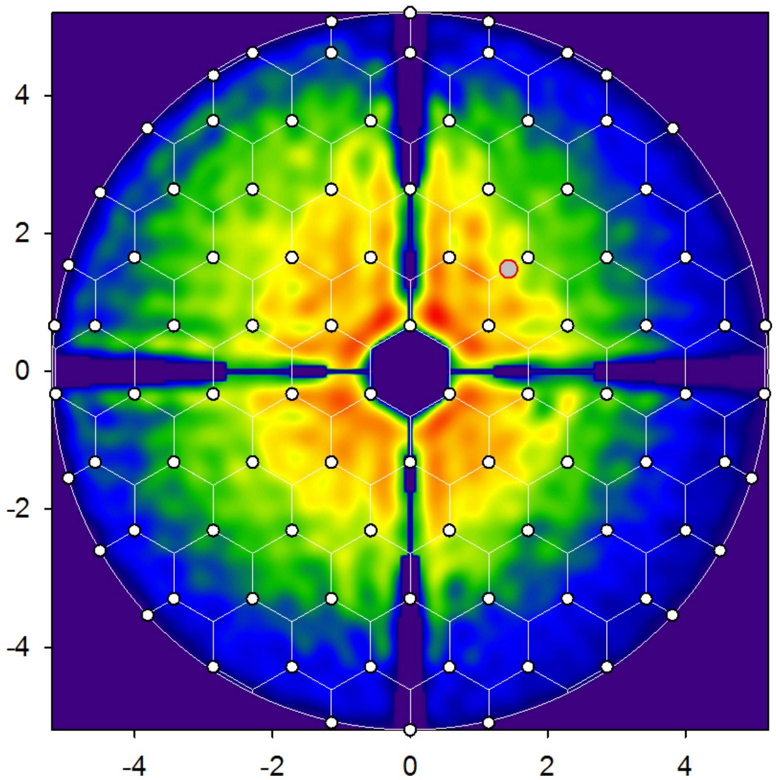

C4 field amplitude

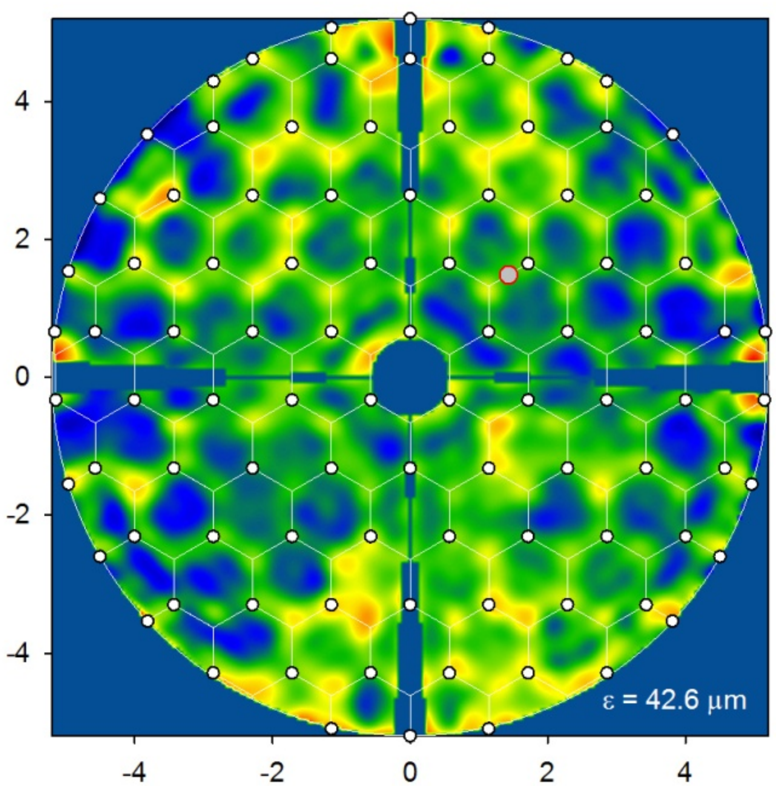

C4 surface error

Fig. 9.— Cont’d

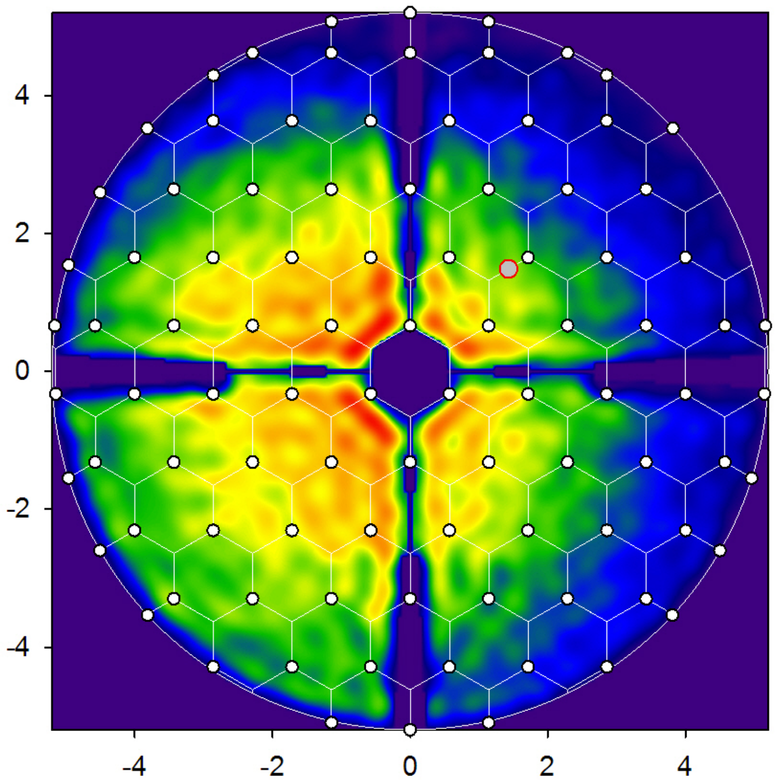

C5 field amplitude

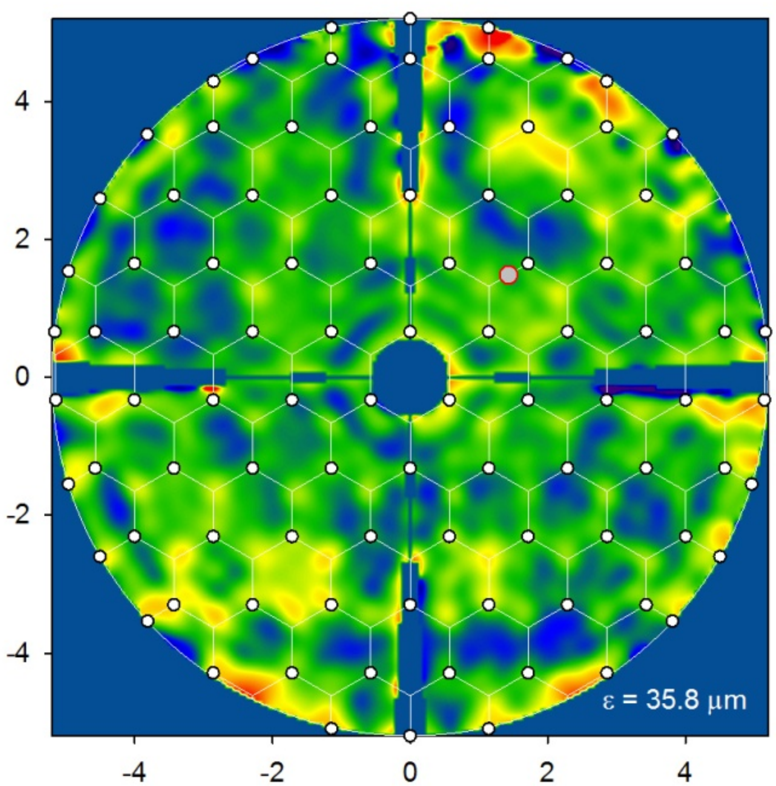

C5 surface error

Fig. 9.— Cont'd

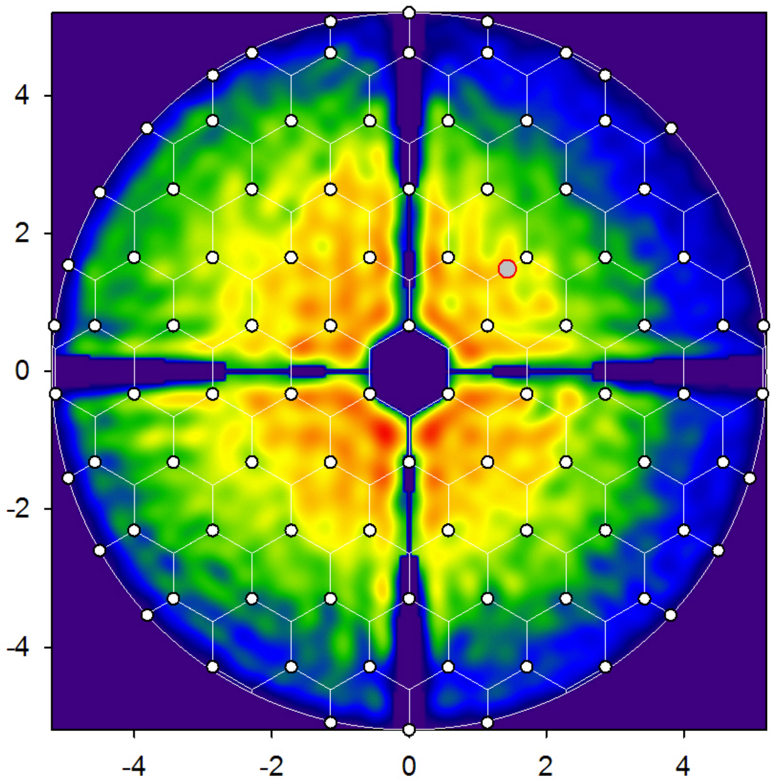

C6 field amplitude

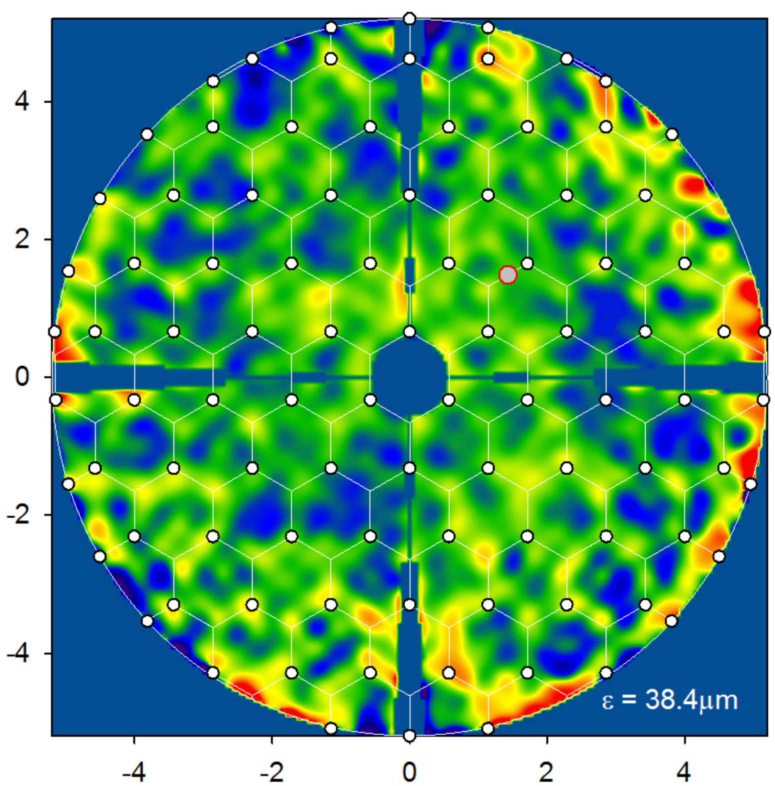

C6 surface error

Fig. 9.— Cont'd

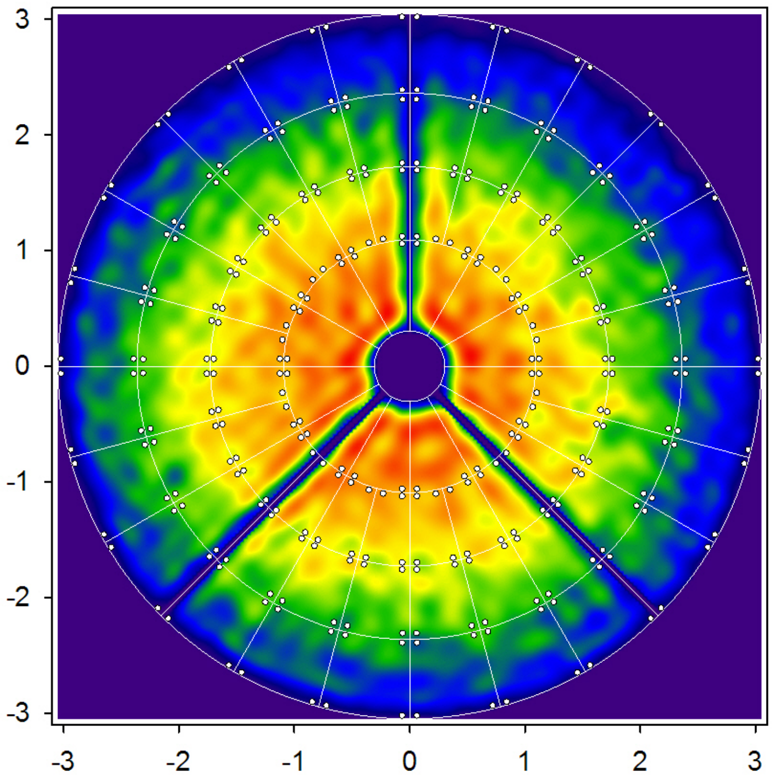

C7 field amplitude

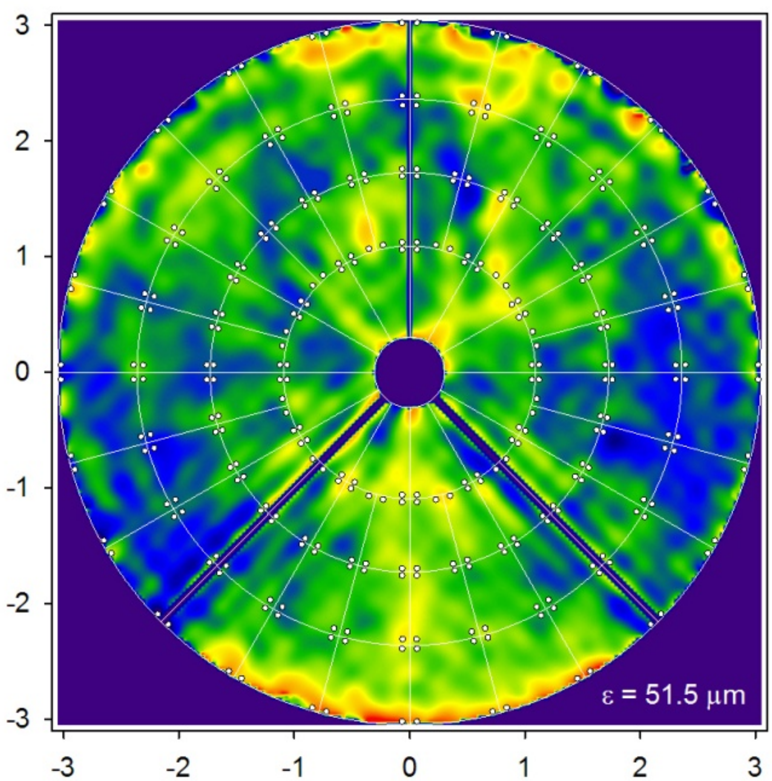

C7 surface error

Fig. 9.— Cont’d

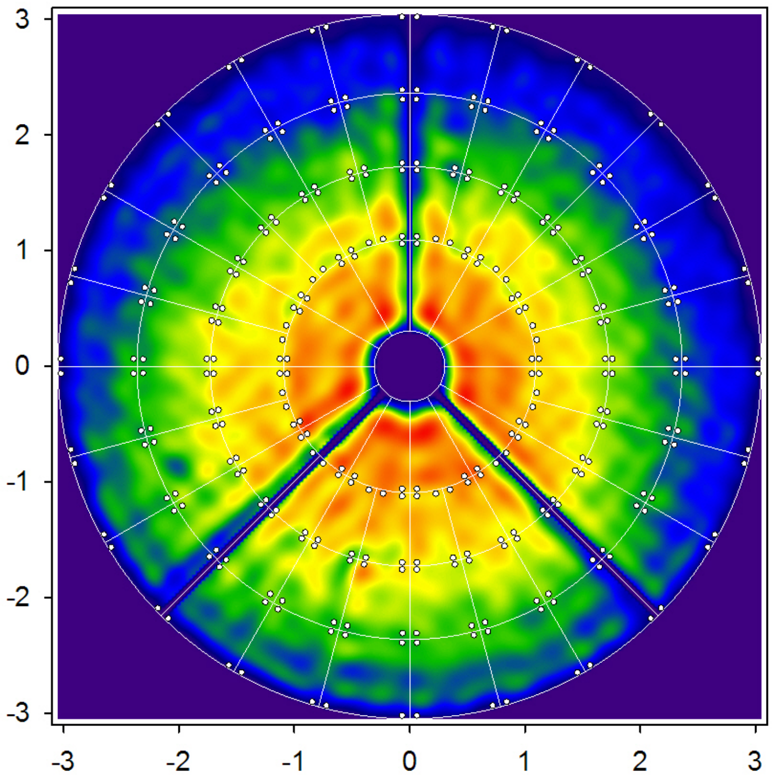

C8 field amplitude

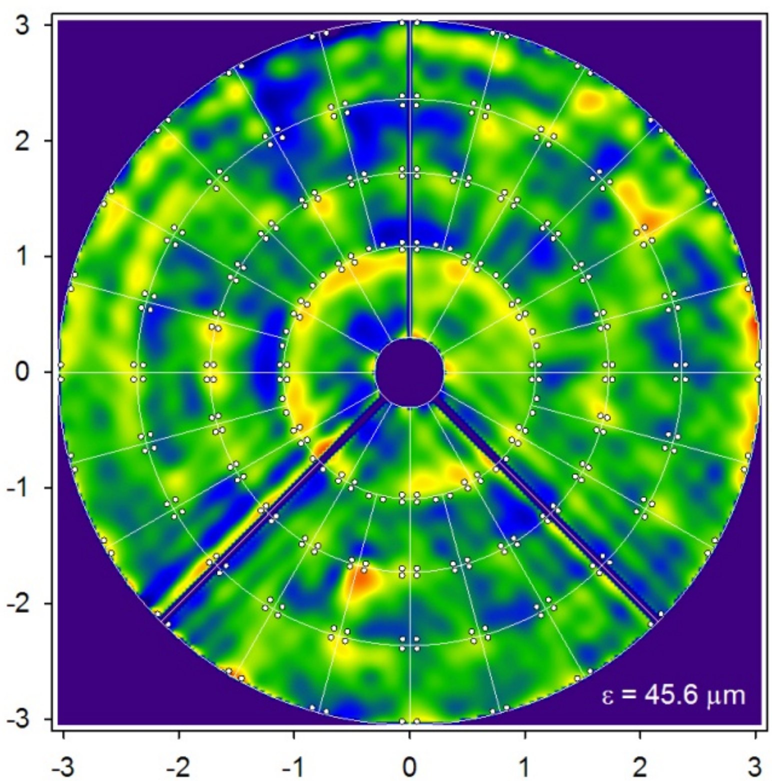

C8 surface error

Fig. 9.— Cont'd

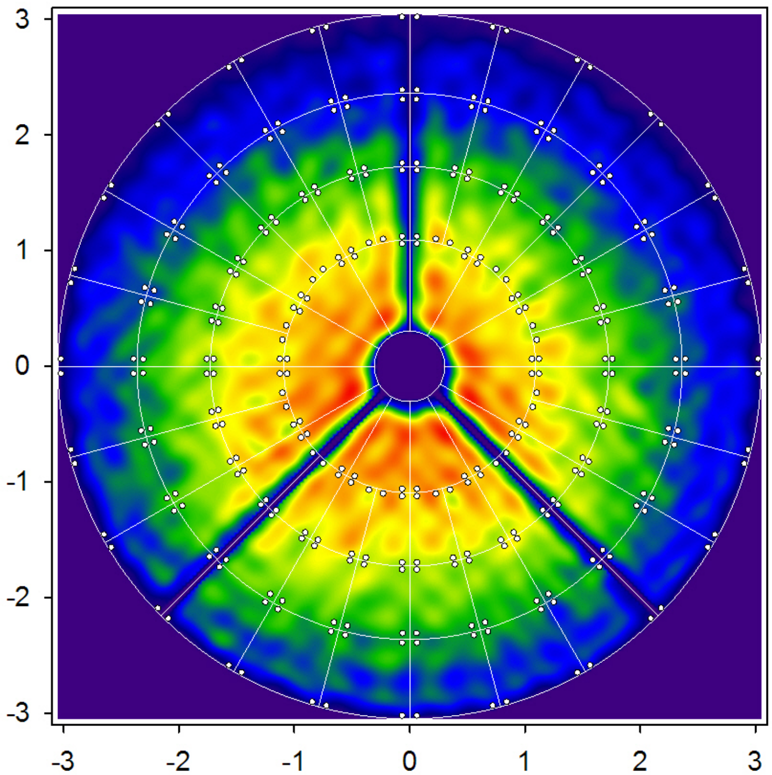

C9 field amplitude

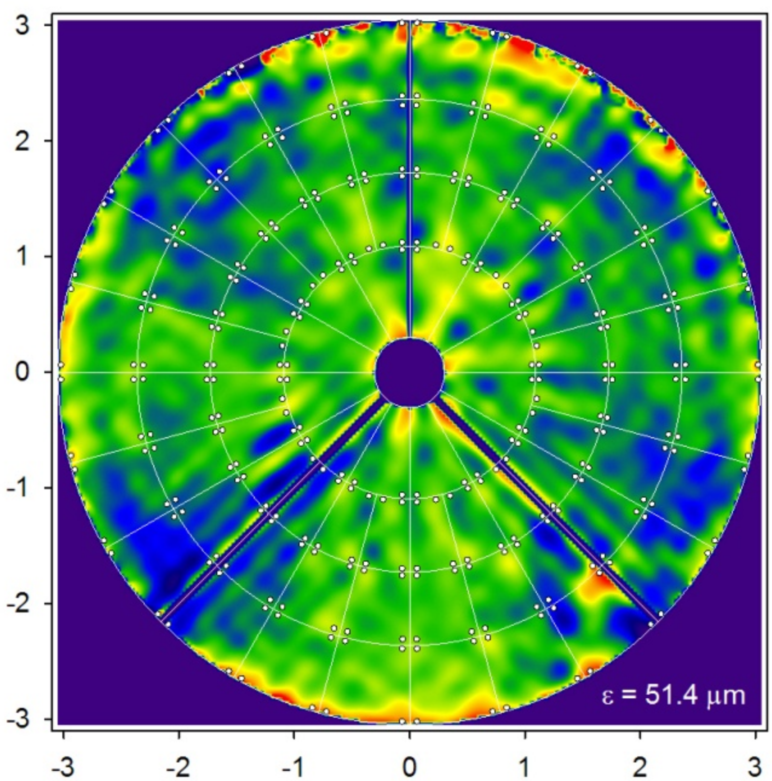

C9 surface error

Fig. 9.— Cont'd

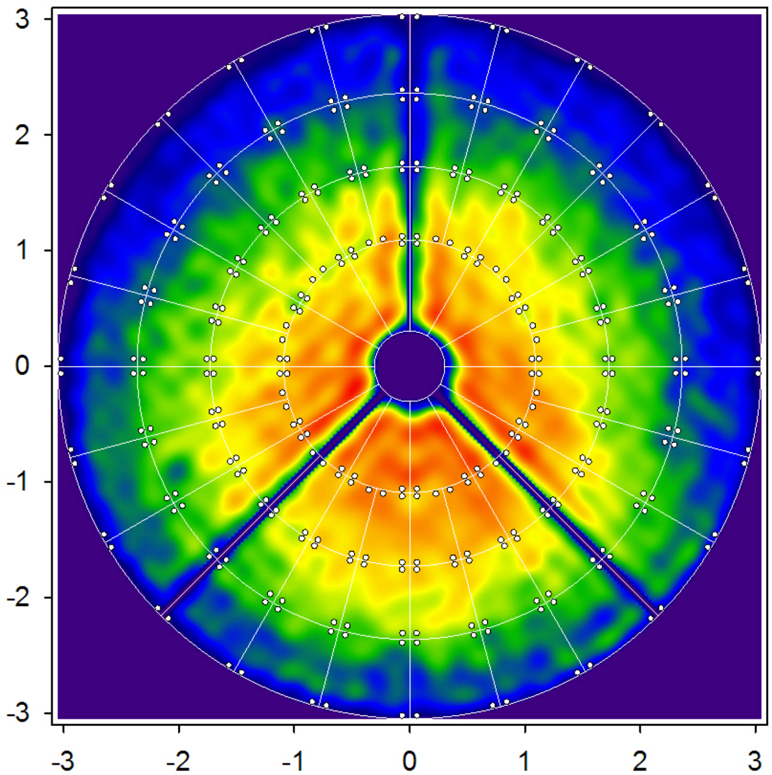

C10 field amplitude

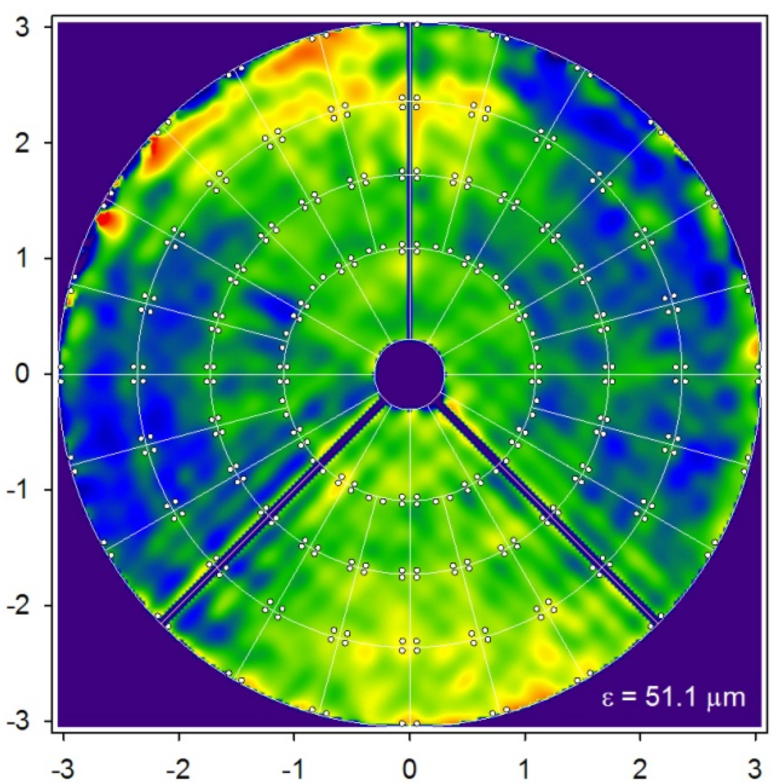

C10 surface error

Fig. 9.— Cont’d

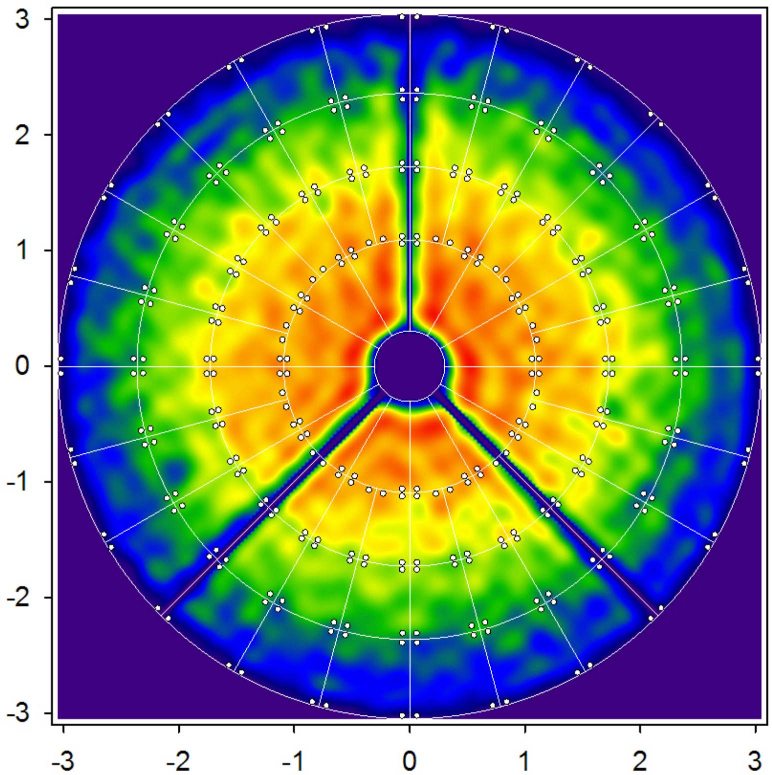

C11 field amplitude

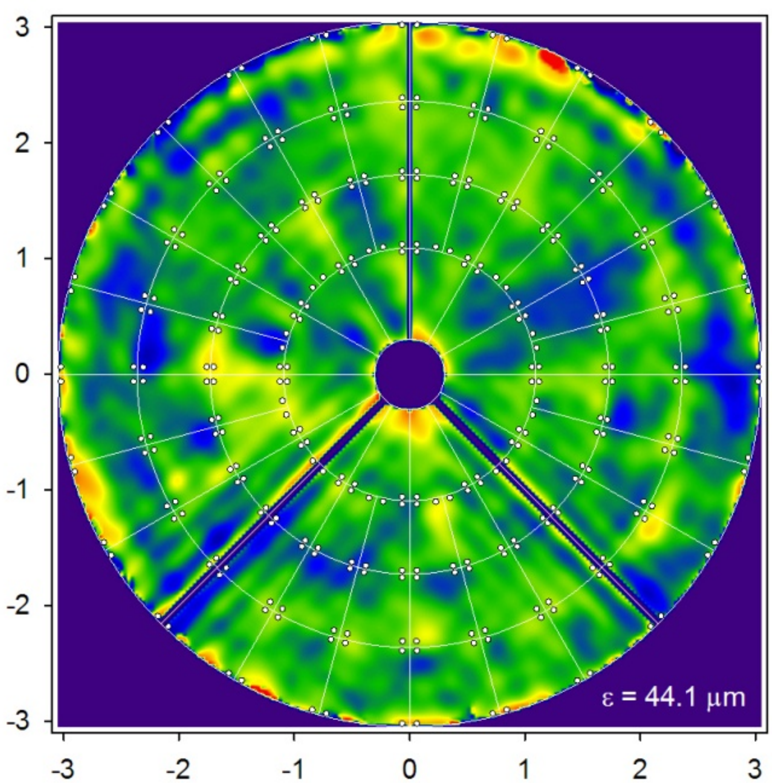

C11 surface error

Fig. 9.— Cont'd

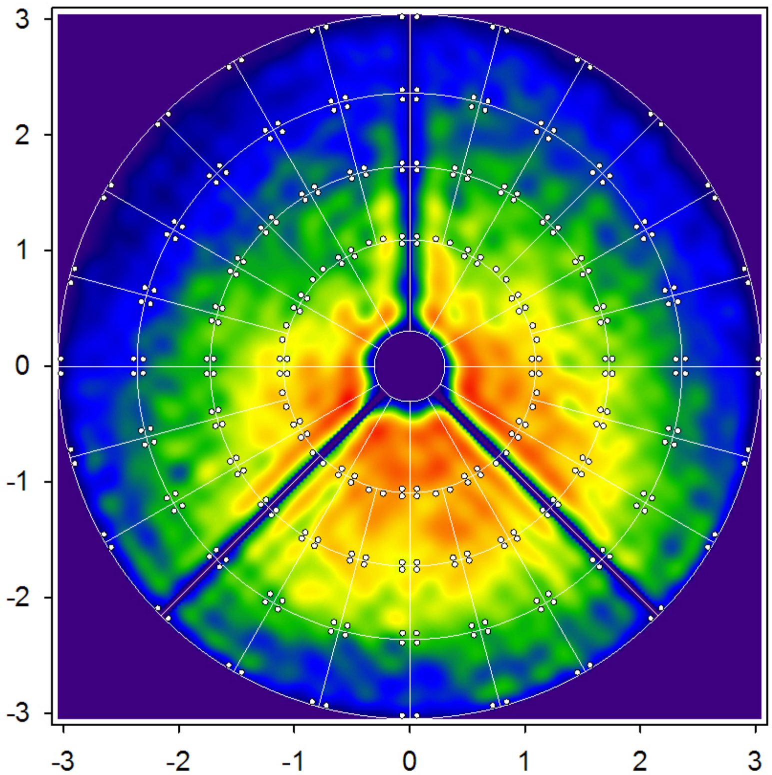

C12 field amplitude

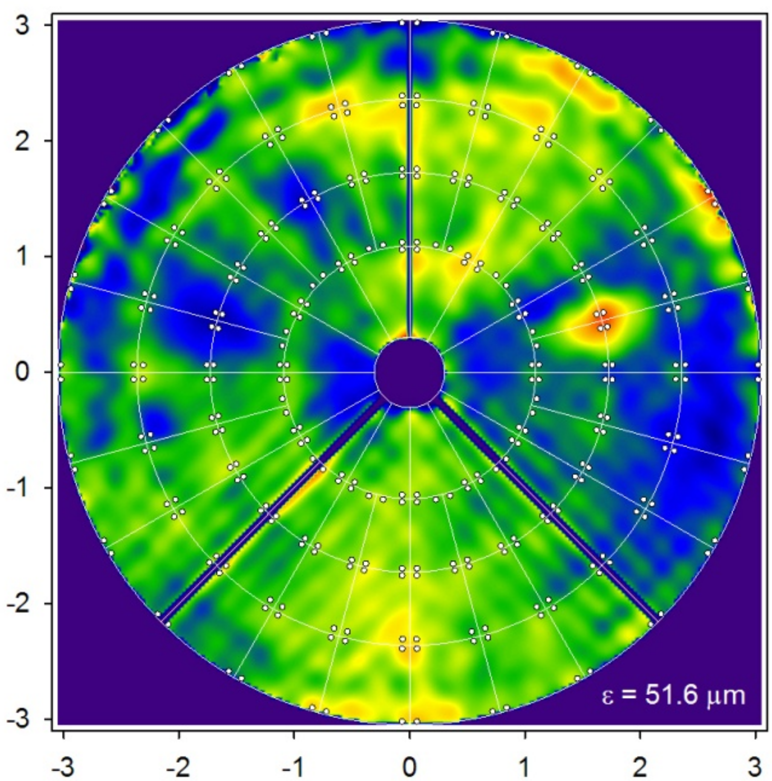

C12 surface error

Fig. 9.— Cont'd

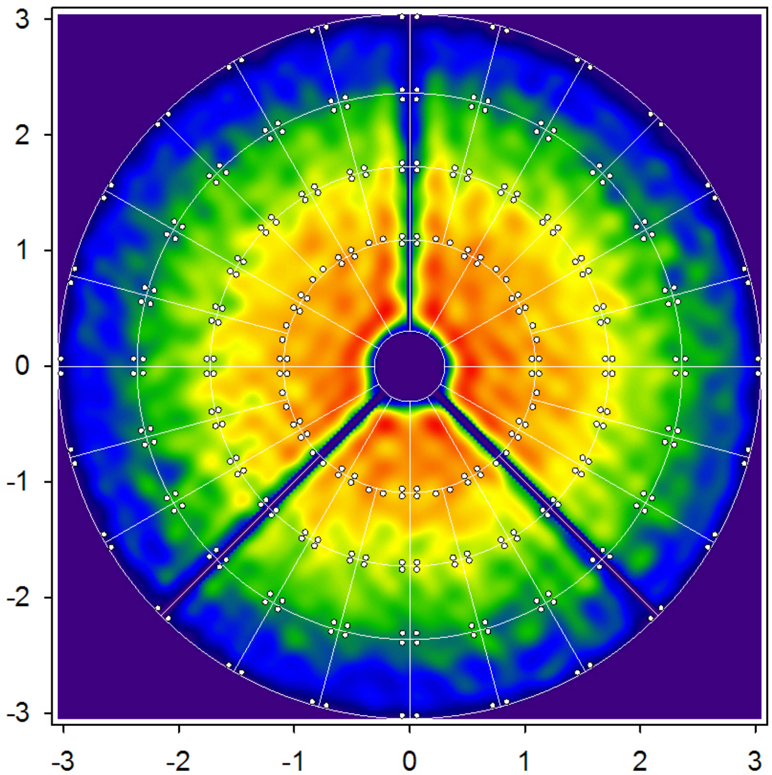

C13 field amplitude

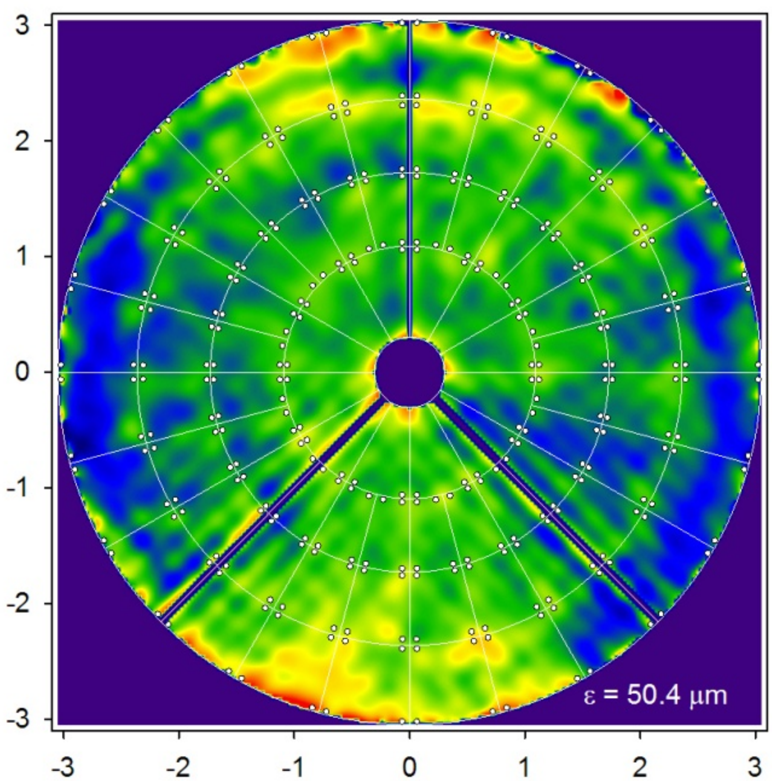

C13 surface error

Fig. 9.— Cont'd

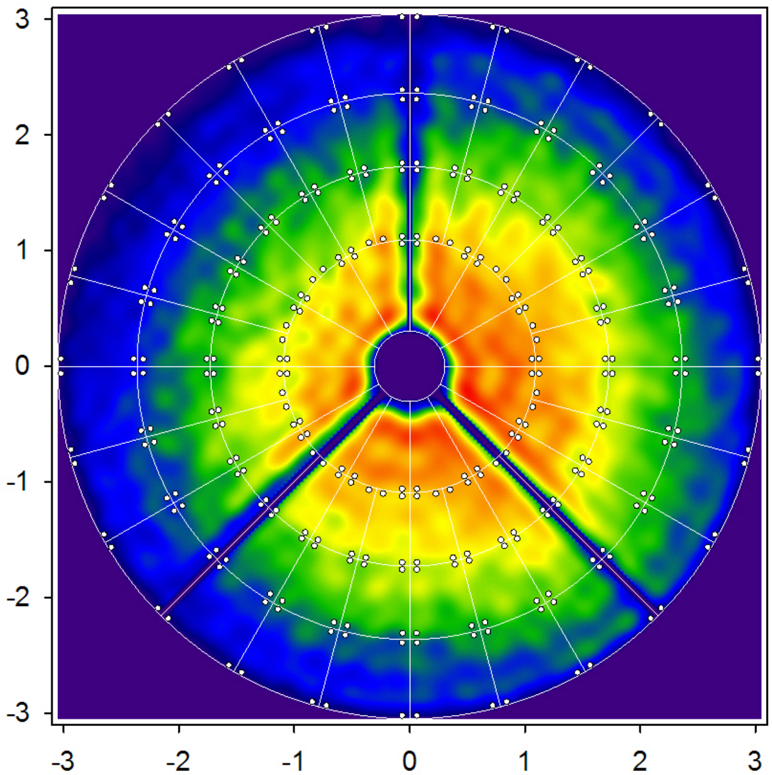

C14 field amplitude

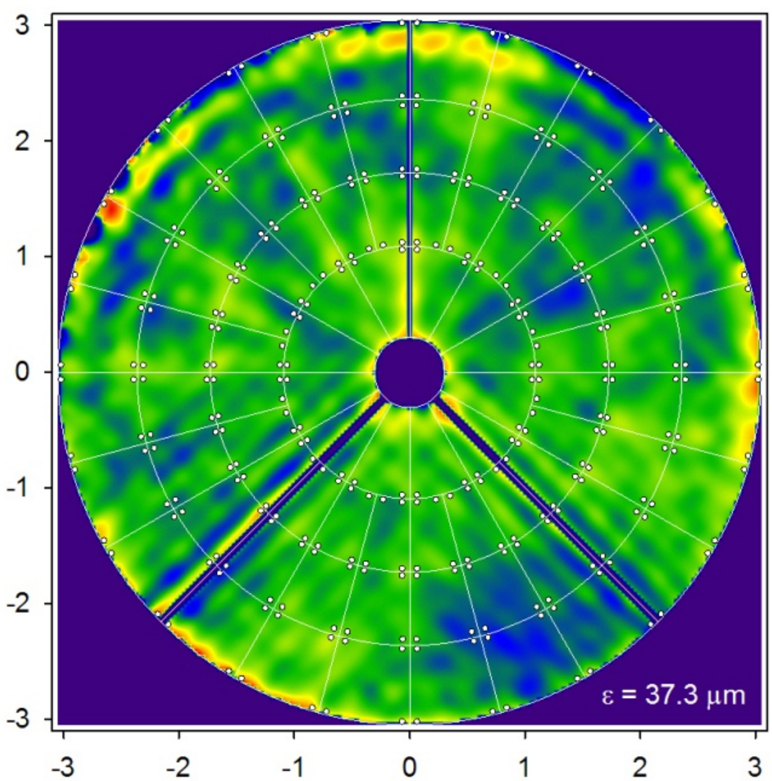

C14 surface error

Fig. 9.— Cont'd

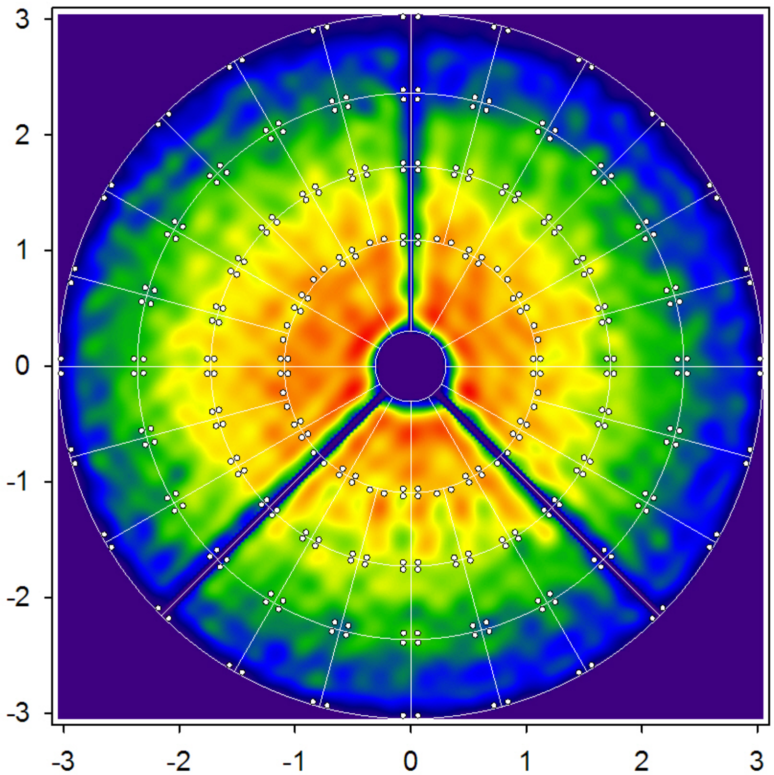

C15 field amplitude

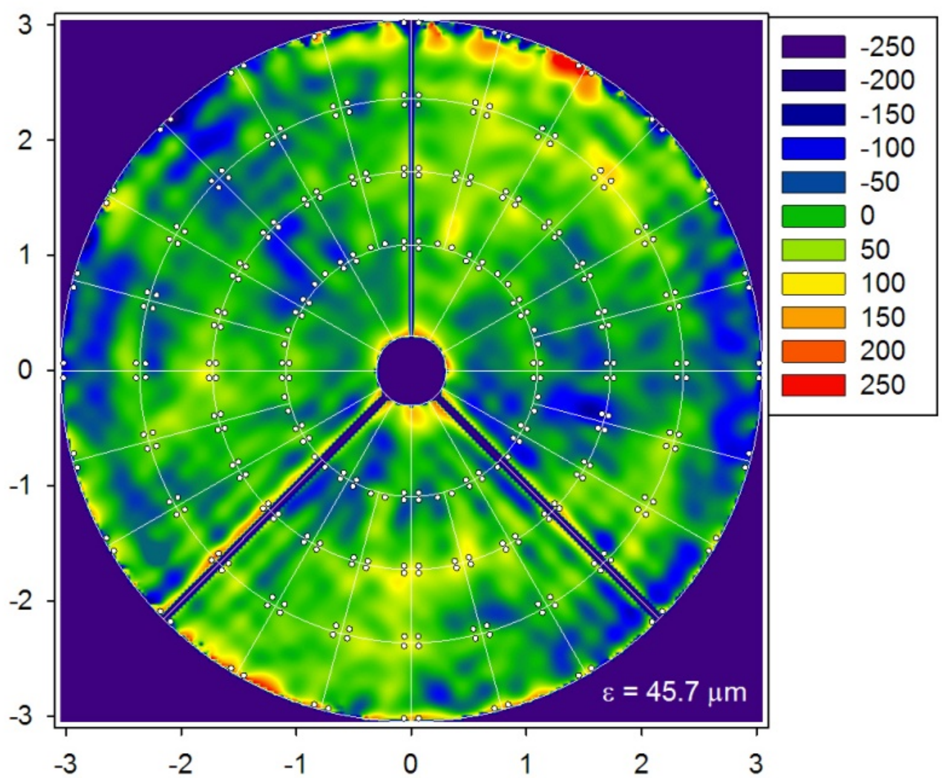

C15 surface error

Fig. 9.— Cont’d

5.4.1 Pointing

Fits of the linear tilt of the phase in the aperture give a measure of the average pointing offset over the holography observation. Although a large fixed pointing offset should not in principle affect the final determination of the surface, good pointing is preferred since it minimizes the sensitivity of the central pointing observations to tracking errors. Every holography run starts with a pointing measurement on the target source so the residual errors reported below are all small, as expected.

Table 4 gives the derived pointing offsets for the various runs. The OVRO antennas are typically within a tenth of a beam, and the BIMA antennas have slightly larger deviations.

Table 4: Pointing offsets derived from the path error maps for each of the observations.

Ant.	Run	$\delta\theta_x$ arcmin	$\delta\theta_y$ arcmin	$\lvert\delta\theta\rvert$ arcmin	$\frac{\lvert\delta\theta\rvert}{1.22\lambda/D}$
C1	30-Jun-08	0.094	–0.001	0.094	0.074
	10-Jul-08	0.046	0.010	0.047	0.037
	22-Jul-08	0.085	–0.059	0.103	0.081
	3-Aug-08	–0.074	–0.047	0.088	0.069
C2	3-Aug-08	–0.077	–0.044	0.089	0.070
	29-Aug-08	0.004	–0.054	0.054	0.043
C3	11-Aug-08	–0.058	–0.098	0.114	0.089
C4	11-Aug-08	–0.091	–0.059	0.108	0.085
	29-Aug-08	–0.092	–0.098	0.134	0.106
C5	27-Jul-08	–0.080	–0.037	0.088	0.069
	29-Aug-08	–0.004	–0.059	0.059	0.046
C6	27-Jul-08	–0.082	0.003	0.082	0.064
		–0.027	–0.045	0.088	0.069
C7	20-Aug-08	–0.310	–0.035	0.312	0.144
C8	19-Aug-08	–0.279	–0.110	0.300	0.138
C9	20-Aug-08	–0.101	–0.177	0.204	0.094
C10	19-Aug-08	–0.013	–0.084	0.085	0.039
C11	20-Aug-08	–0.265	–0.184	0.323	0.149
C12	19-Aug-08	–0.168	0.048	0.175	0.080
C13	20-Aug-08	–0.228	–0.285	0.365	0.168
C14	19-Aug-08	–0.136	–0.006	0.136	0.063
C15	20-Aug-08	–0.281	–0.201	0.345	0.159
		–0.198	–0.115	0.249	0.115

5.4.2 Illumination Offset

Offsets of the illumination on the primary mirror were estimated by fitting a function to represent the ideal feed pattern, imaged on to the antenna aperture:

$$E(x,y) = E_0 J_0^T\left(\frac{\sqrt{(x-x_0)^2+(y-y_0)^2}}{r_0} j_{01}\right), \tag{22}$$

where (x_0, y_0) is the offset of the illumination of the primary, E_0 is an amplitude normalization, r_0 is a scale parameter that controls the illumination taper, and j_{01} is the first root of the zeroth order Bessel function, J_0. The superscript on the Bessel function indicates that it is truncated at its first null and considered zero outside that. Each spectral window (with all baselines averaged) was fitted separately and the average and RMS of the fits are shown in Table 5. The corresponding edge tapers derived from the average of the widths are 9.7 dB (OVRO) and 9.8 dB (BIMA).

Table 5: Offsets obtained for the aperture illumination patterns.

Ant.	Run	Δx, m	σ, m	Δy, m	σ, m	r_0, m	σ, m
C1	30-Jun-08	0.23	0.03	–0.34	0.15	6.36	0.11
	10-Jul-08	0.26	0.04	–1.12	0.07	6.94	0.09
	22-Jul-08	0.10	0.02	–1.16	0.04	6.94	0.09
	3-Aug-08	0.10	0.02	–0.72	0.07	6.99	0.12
C2	3-Aug-08	0.18	0.11	0.53	0.08	6.92	0.08
	29-Aug-08	0.02	0.12	–0.21	0.02	7.11	0.10
C3	11-Aug-08	–0.37	0.05	0.24	0.11	7.10	0.16
C4	11-Aug-08	–0.08	0.03	0.30	0.02	6.76	0.07
	29-Aug-08	–0.37	0.04	0.22	0.03	6.65	0.10
C5	27-Jul-08	–0.85	0.06	–1.03	0.28	7.14	0.22
	29-Aug-08	–0.82	0.08	0.55	0.03	6.77	0.11
C6	27-Jul-08	–0.43	0.13	–0.69	0.07	6.96	0.13
					Mean:	**6.85**	**0.008**
C7	20-Aug-08	–0.16	0.01	–0.16	0.06	4.04	0.05
C8	19-Aug-08	–0.11	0.02	–0.29	0.04	4.11	0.10
C9	20-Aug-08	–0.10	0.02	–0.33	0.05	3.96	0.03
C10	19-Aug-08	0.02	0.02	–0.32	0.06	4.10	0.08
C11	20-Aug-08	–0.02	0.02	0.01	0.05	4.09	0.05
C12	19-Aug-08	0.17	0.03	–0.50	0.07	4.21	0.13
C13	20-Aug-08	0.06	0.03	–0.12	0.05	4.03	0.06
C14	19-Aug-08	0.29	0.01	–0.17	0.07	3.95	0.05
C15	20-Aug-08	–0.14	0.03	–0.03	0.05	4.15	0.13
					Mean:	**4.01**	**0.005**

5.4.3 Focus

Focusing offsets derived from the fit are given in Table 6. In a couple of cases the focus was offset from the normal observing values as indicated, but all other values were the ones in routine use. Offsets in x and y are small enough to be ignored, but some antennas needed to be refocused in the z direction. Repeatability appears to be at the level of 0.2 mm.

On 20 September 2008 an interferometric aperture efficiency measurement was made using 3C454.3, and, following a correction for the z focus of several antennas, a second measurement was made. The efficiency measurements, including pointing at λ3-mm, took about 20 min each. Measurements of the flux of 3C454.3 from 19 and 21 September 2008 [5] were interpolated to 20 September with a resulting value of 25.3 Jy. Table 7 presents the results of the measurement, showing a systematic and significant improvement in the efficiency for the antennas that had their z focus adjusted.

Although the results are not as clear-cut as hoped, in that the improvement is not as high as expected given the focus changes, they are generally encouraging.

Table 6: Focus corrections and associated surface errors. The seventh and eighth columns give the contribution to the total surface error from the lateral (*x* and *y*) and axial (*z*) focal offsets.

		Focus			Effective surface error			
		x	y	z	Initial	Lateral	Axial	Final
Ant.	Run	mm	mm	mm	μm	μm	μm	μm
C1	30-Jun-08	–0.526	–0.499	–0.157[a]	111.4	11.6	106.7[a]	30.1
	10-Jul-08	–0.403	–1.050	0.276	41.3	17.9	18.8	32.0
	22-Jul-08	–0.435	–0.357	–0.125	45.5	9.0	8.5	43.7
	3-Aug-08	–0.640	–0.611	0.308	38.4	14.1	21.0	28.9
C2	3-Aug-08	–0.730	–0.132	0.601	56.1	11.8	40.9	36.5
	29-Aug-08	–0.716	–0.015	0.966[a]	75.3	11.4	65.9[a]	34.6
C3	11-Aug-08	–0.669	0.472	–0.398	44.1	13.0	27.1	32.2
C4	11-Aug-08	–0.395	0.321	0.324	49.3	8.1	22.1	43.4
	29-Aug-08	–0.272	–0.026	0.257	46.3	4.3	17.5	42.6
C5	27-Jul-08	–0.714	0.126	0.060	66.1	11.6	4.1	65.0
	29-Aug-08	–0.560	0.270	0.017	37.1	9.9	1.2	35.8
C6	27-Jul-08	–0.796	0.922	0.401	51.1	19.3	27.3	38.6
C7	20-Aug-08	0.144	0.136	–0.057	51.8	3.5	4.2	51.5
C8	19-Aug-08	–0.181	0.239	–0.319	51.6	5.3	23.6	45.6
C9	20-Aug-08	–0.363	–0.161	–0.984	89.3	7.0	72.6	51.4
C10	19-Aug-08	0.477	0.920	–0.310	58.9	18.2	22.9	51.1
C11	20-Aug-08	0.228	–0.164	–0.947	82.8	4.9	69.9	44.1
C12	19-Aug-08	0.524	0.640	0.540	66.8	14.5	39.9	51.6
C13	20-Aug-08	0.644	0.693	–0.077	53.4	16.6	5.7	50.4
C14	19-Aug-08	0.346	0.166	0.537	54.9	6.7	39.6	37.3
C15	20-Aug-08	–0.002	0.346	–0.514	59.7	6.1	38.0	45.7

[a] Focus offset from normal observing value

Table 7: Results of focus adjustment on 20 September 2008. Efficiency measurements were made on 3C454.3. The average ratio for all antennas that were not refocused was $\eta_1/\eta_2 = 0.995$.

Ant.	η_1, %	η_2, %	Δz	$\frac{\eta_2}{\eta_1}$
C1	66.5	65.8		0.989
C2	54.8	57.2	0.601	1.044
C3	45.9	44.2		0.963
C4	66.3	65.3		0.985
C5	60.2	61.6		1.023
C6	45.5	45.3		0.996
C7	68.7	69.3		1.009
C8	56.8	55.3		0.974
C9	38.8	67.9	-0.984	1.750
C10	45.5	45.8		1.007
C11	48.0	69.2	-0.947	1.442
C12	52.3	59.2	0.540	1.132
C13	69.0	69.4		1.006
C14	64.4	69.9	0.537	1.085
C15	59.8	60.3	-0.514	1.008

5.4.4 Surface Error

Once the antennas have been refocused according to Table 6, the surface errors of all the antennas appear to be reasonable. The maximum loss of efficiency at 250 GHz is about 24 % relative to a perfect surface. Averaging the best maps for all of the OVRO antennas in quadrature yields a value of 32 μm, and for the BIMA antennas gives 42 μm.

Inspection of the surface error maps indicates that several should be improved with some adjustments. Primarily, antennas …

C1: This antenna has a very good surface figure. Although there are some ring features evident these do not correspond in any obvious way to the structure and so may be artifacts of the measurement.

C2: There are a few features that correspond to panel edges that can possibly be improved. It is not clear if the relatively large phase error round the top of the dish is real or not.

C3: Generally a good surface with one panel that has a significant error.

C4: Clear features on many panels, indicating that the panel curvature does not match the desired curvature of the surface. These could be corrected only by deforming the panels and not by adjustment of the supports.

C5: A good surface with a few individual panel features, but no obvious adjuster errors.

C6: Also has no obvious possibility for support adjustment as the errors appear mainly internal to the panels.

C7: This antenna has one of the highest surface errors, with two areas on the left and right below the centerline being systematically low. This is a good candidate for surface adjustment.

C8: This antenna has a number of panels that could be adjusted to give a useful increase in efficiency.

C9: The surface error has a quadrupole type of distribution with low points along the intercardinal lines. Particularly in the lower-left there are several obvious areas where panels can be readjusted, which will be worthwhile since this antenna has one of the highest surface RMS values.

C10: This antenna also has one of the highest surface errors with the deviations in large regions that can be adjusted.

C11: Some of the errors in this antenna are at panel edges and so can probably be removed. There also appears to be a ring of errors on the outer panel that would not be taken out by the adjusters.

C12: Another antenna with a high surface error and regions that are clearly amenable to improvement.

C13: Like C11, this antenna also appears to have errors in a circular pattern on the outer ring of panels. Since the surface error is so high it needs to be investigated in more detail.

C14: One of the best surfaces.

C15: A moderately good surface with a few potential adjustment areas.

In Fig. 10 we show the effect of the surface errors as a function of frequency for the range of errors that the holography results span. Clearly surface deviations of less than 50 μm are highly desirable, and values of less than 40 μm would be a good goal.

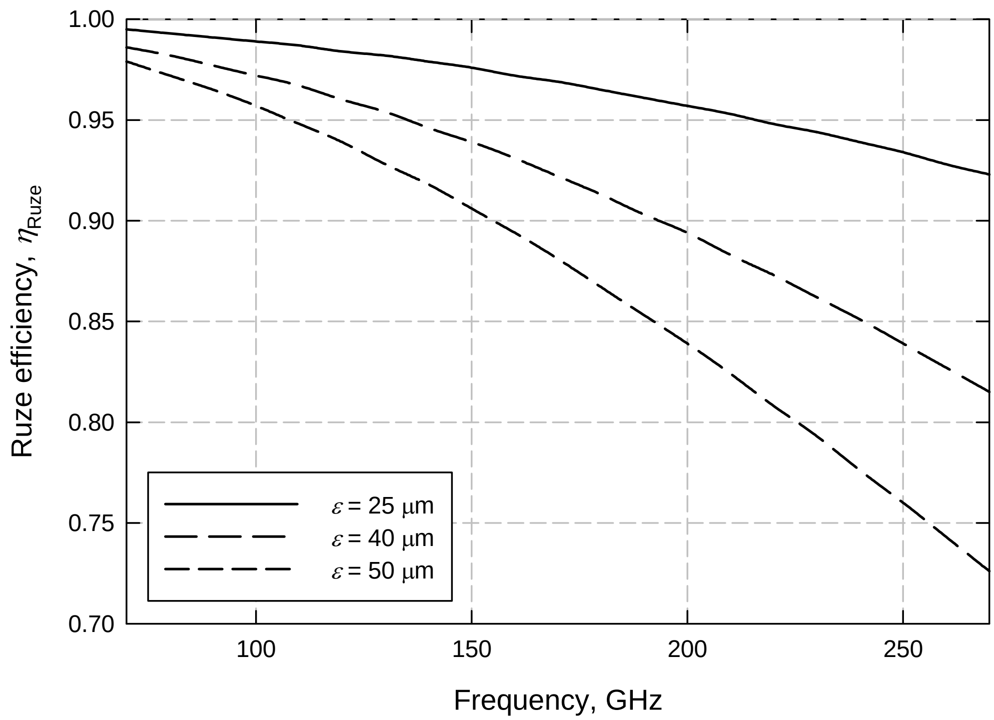

Fig. 10.— Ruze efficiency loss for approximately the range of surface errors of the CARMA antennas over the observing frequency range.

6 Conclusions

High quality holographic measurements of the surfaces of the OVRO and BIMA antennas were obtained during the summer of 2008. We have developed an analysis procedure that allows the data to be rapidly reduced to evaluate the performance of the antennas. Maps of 41×41 points were made, giving a good view of the surfaces with a resolution of several points per panel. The final statistical uncertainties in the maps is probably around 10–20 μm.

In general, the antenna surfaces appear to be remarkably good considering that all the antennas were disassembled and reassembled at the CARMA site after transportation. In general, the OVRO antennas appear to have somewhat better surfaces than the BIMA antennas.

Our analysis also provides estimates of the adjustments needed to refocus the secondary mirrors, and this was applied to one OVRO and five BIMA antennas with some significant improvement in efficiency. We have not yet adjusted any of the surfaces, but there are several cases where some alignment is indicated.

7 Appendices

7.1 Assumed Antenna Optical Parameters

For reference, we record the assumed values for some of the relevant antenna-dependent parameters used in the calculations in Table 8.

Table 8: Parameters used in the calculations described in the memo.

Parameter	Symbol	Value, m OVRO	 BIMA	 SZA
Primary diameter	D	10.40	6.10	3.50
Secondary diameter	d_s	0.610	0.610	0.350
Primary focal length	f_p	4.1233	2.5603	1.225
El axis to dish mid-plane	d_a	4.0	2.0	1.0

7.2 Ruze Aberration Formulas

In an unpublished but widely used memo [6], Ruze presents the path errors that result from displacements of the feed or secondary mirror in Cassegrain and Gregorian antennas. Table 9 lists the appropriate equations which contain an arbitrary offset to make the error zero at the center of the aperture. A motion of the secondary mirror can be viewed as a displacement of the secondary and feed as a single unit, followed by an opposite movement of the feed to return it to its nominal focus. All the errors for the secondary motion are therefore the sum of a prime focus feed displacement and a secondary focus one.

Table 9: Path length error resulting from various displacements and tilts of the feed and secondary mirror. **Note:** the path length error is considered *positive* if the path length is *reduced*, and *negative* if the path length is *increased*. This means that a positive path length error corresponds to a positive phase.

Position Error	Path Length Error
Feed axial displacement, Δz_f	$\Delta z_f \cos\theta_f$
Feed lateral displacement, $\Delta r_f,\ \phi_0$	$\Delta r_f \cos(\phi - \phi_0)\sin\theta_f$
Secondary mirror axial displacement, Δz_s	$-\Delta z_s\left(\cos\theta_p + \cos\theta_f\right)$
Secondary mirror lateral, $\Delta r_s,\ \phi_0$	$\Delta r_s \cos(\phi - \phi_0)\left(\sin\theta_p - \sin\theta_f\right)$
Secondary mirror tilt, $\Delta\alpha, \phi_0$	$-(c-a)(\Delta\alpha_x \sin(\phi - \phi_0))\left(\sin\theta_p + M\sin\theta_f\right)$
where	$\sin\theta_p = \dfrac{\frac{r}{f}}{1+\left(\frac{r}{2f}\right)^2}$ $\sin\theta_f = \dfrac{\frac{r}{Mf}}{1+\left(\frac{r}{2Mf}\right)^2}$

In principle, a measurement of the aperture field phase can yield both the secondary mirror and feed displacements. Practically, however, there is some degeneracy between the two, and the feed errors are significantly smaller than the secondary mirror errors (by $\sim M^2$ or higher). There is generally not enough accuracy in the data to separate them. Here we choose to completely ignore the feed error and retain only the terms in $\cos\theta_p$ and $\sin\theta_p$, which can be shown to lead to negligibly small errors. Under this assumption, it is found that the secondary mirror tilts are degenerate with the displacements, so we may further restrict ourselves to only three translations of the secondary.

Some other modifications to the formulas are required before we apply them to the data. An average value is removed from each of the three aberrations before fitting them (and also from the data, before fitting). A constant offset in path length has no effect on the beam pattern, but it would lead to erroneous values for the coefficients in (13) when the integral was evaluated. The lateral offset path errors have large linear terms that correspond to pointing offsets. This linear component cannot be used to determine the radial offset of the secondary, however, since there is no absolute reference for the antenna pointing direction. Therefore we remove the linear term from the expression, leaving only the comatic aberration, and fit the pointing term separately.

Following Ruze, we define a beam deviation factor that is the ratio of the shift of the main beam, $\Delta\theta$, to the change in angle of the axis from the prime focus of the secondary to the primary vertex, $\Delta \mathrm{r}/f_p$, when the secondary is shifted radially by Δr. This is calculated as

$$BDf = \frac{f_p \int_0^{D/2} \sin\theta_p \, r^2 dr}{\int_0^{D/2} r^3 dr} \tag{23}$$

The path length error terms that are used in (13) are then

$$p_{\alpha x} = y\,, \tag{24}$$

$$p_y = -x\,, \tag{25}$$

$$p_{\Delta \mathrm{x}} = -\cos(\phi)\sin\theta_p + BDf\,\frac{x}{f_p} - \overline{p_{\Delta \mathrm{x}}}\,, \tag{26}$$

$$p_{\Delta \mathrm{y}} = -\cos(\phi)\cos\theta_p + BDf\,\frac{y}{f_p} - \overline{p_{\Delta \mathrm{y}}}\,, \tag{27}$$

$$p_{\Delta z} = -\cos\theta_p\,, \tag{28}$$

where the overbar denotes the value to subtract to give a zero mean to the integral. The total path error is then

$$p = \alpha_x\, p_{\alpha x} + \alpha_y\, p_{\alpha y} + \Delta x\, p_{\Delta x} + \Delta y\, p_{\Delta y} + \Delta z\, p_{\Delta z} + p_{surf}\,. \tag{29}$$

When these expressions are evaluated in (15) the integrals are replaced by sums over the grid of data points in the unblocked areas of the aperture.

Sensitivity to the effects of displacements of the secondary can be evaluated by calculating the RMS path length error (with zero mean) over the aperture. All three CARMA antenna types have similar focal ratios, so their sensitivities to secondary mirror misalignments are similar, as is evident from Table 10. Although we do not show the expressions here, the errors can be weighted by the amplitude of the aperture field [6], and the results are included in Table 10. The effect of the weighting is very minimal.

Table 10: Equivalent surface errors arising from secondary mirror focal position errors.

Antenna	Axial error μm.mm^{-1}		Radial Error μm.mm^{-1}	
	Unweighted	Weighted	Unweighted	Weighted
OVRO	82	79	20	19
BIMA	75	73	17	16
SZA	96	94	26	25

8 References

[1] S. Corder and M. C. H. Wright, "CARMA holography," CARMA Memo 36, 2006.
[2] E. V. Jull, *Aperture antennas and diffraction theory*. Stevenage: Peter Peregrinus, 1981.
[3] W. V. T. Rusch, "Scattering from a hyperboloidal reflector in a Cassegrainian feed system," *IEEE Trans. Antennas and Propagat.*, vol. AP-11, pp. 414-421, Jul. 1963.
[4] J. Ruze, "Antenna tolerance theory-a review," *Proc. IEEE,* vol. 54, pp. 633-640, Apr. 1966.
[5] J.-P. Macquart, 2008.
[6] J. Ruze, "Small displacements in parabolic reflectors," Massachusetts Institute of Technology, Lincoln Laboratory, Lexington, Massachusetts Feb. 1969.